Available online at www.sciencedirect.com
SCIENCE DIRECT®
Mechanics of Materials 35 (2003) 333–364
MECHANICS OF MATERIALS
www.elsevier.com/locate/mechmat

A grain level model for the study of failure initiation and evolution in polycrystalline brittle materials. Part I: Theory and numerical implementation

Horacio D. Espinosa *, Pablo D. Zavattieri [1]

Department of Mechanical Engineering, Northwestern University, 2145 Sheridan Road, Evanston, IL 60208-3111, USA

Received 17 September 2001; received in revised form 11 April 2002

Abstract

A model is presented to analyze material microstructures subjected to quasi-static and dynamic loading. A representative volume element (RVE) composed of a set of grains is analyzed with special consideration to the size distribution, morphology, chemical phases, and presence and location of initial defects. Stochastic effects are considered in relation to grain boundary strength and toughness. Thermo-mechanical coupling is included in the model so that the evolution of stress induced microcracking, from the material fabrication stage, can be captured. Intergranular cracking is modeled by means of interface cohesive laws motivated by the physics of breaking of atomic bonds or grain boundary sliding by atomic diffusion. Several cohesive laws are presented and their advantages in numerical simulations are discussed. In particular, cohesive laws simulating grain boundary cracking and sliding, or shearing, are proposed. The equations governing the problem, as well as their computer implementation, are presented with special emphasis on selection of cohesive law parameters and time step used in the integration procedure. This feature is very important to avoid spurious effects, such as the addition of artificial flexibility in the computational cell. We illustrate this feature through simulations of alumina microstructures reported in part II of this work. A technique for quantifying microcrack density, which can be used in the formulation of continuum micromechanical models, is addressed in this analysis. The density is assessed spatially and temporally to account for damage anisotropy and evolution. Although this feature has not been fully exploited yet, with the continuous development of cheaper and more powerful parallel computers, the model is expected to be particularly relevant to those interested in developing new heterogeneous materials and their constitutive modeling. Stochastic effects and other material design variables, although difficult and expensive to obtain experimentally, will be easily assessed numerically by Monte Carlo grain level simulations. In particular, extension to three-dimensional simulations of RVEs will become feasible.

* Corresponding author. Tel.: +1-847-467-5989; fax: +1-847-491-3915.
E-mail address: espinosa@northwestern.edu (H.D. Espinosa).
URL: http://www.mech.northwestern.edu/espinosa
[1] Present address: General Motors Research and Development Center, 30500 Mound Road, Warren, MI 48090-9055, USA.

1. Introduction

Accurate modeling of inelasticity and failure of brittle materials is key to the design of microelectronic devices, machining of ceramics and ceramic composites, design of microelectromechanical

0167-6636/03/$ - see front matter © 2002 Elsevier Science Ltd. All rights reserved.
PII: S0167-6636(02)00285-5

systems and armor systems. Many theories have been developed at various size scales from homogenized solids to grain level and atomistic modeling. In this article we present the details and features of the grain level model developed by Espinosa and co-workers in their study of dynamic failure of brittle materials.

A variety of continuum damage models have been developed over the last decade (Bazant and Oh, 1985; Addessio and Johnson, 1999; Curran et al., 1990; Espinosa, 1995; Johnson and Holmquist, 1992). These models are based on homogenizing the cracked solid and finding its response by degrading the elasticity of the material. The fundamental assumption in these models is that inelastic strains are caused by microcracks, whose evolution during loading degrades the strength of the material. This degradation is defined in terms of reduced moduli whose evolution, under compressive, tensile, and mixed loading, is formulated using the generalized Griffith criteria. In addition, some of these models account for the initiation of cracks, coalescence, friction between fragments in the comminuted zone, etc. With the exception of the multiple-plane model, these phenomenological models cannot describe damage induced anisotropy and their parameters are difficult to identify experimentally. Furthermore, these continuum models require assumptions on the initial size and distribution of microcracks and they cannot fully describe the growth of dominant cracks leading to macroscopic failure, which are not suitable to homogenization.

To overcome these limitations, models based on a discrete approach were developed, (Camacho and Ortiz, 1996; Espinosa et al., 1998a; Miller et al., 1999; Xu and Needleman, 1995). In these models, nucleation, propagation and coalescence of cracks during the deformation process is an outcome of the simulation. Discrete models are based on a phenomenological framework where the fracture characteristics of the material are embedded in a cohesive surface traction–displacement relation. Miller et al. (1999) considered models based on energy balance and compared their predictions of fragment size to the results of numerical simulations. They found differences because their energy-based models dealt with the onset of the fragmentation event, but they did not include the time dependence of the process. Therefore, they proposed a model that included the time history of the fragmentation process and parameters, such as the speed of crack propagation and flaw strength distribution.

Within the framework of cohesive interface elements the two most noteworthy cohesive failure models available in the literature are the *intrinsic* exponential potential-based law used by Xu and Needleman (1995), and the *extrinsic* linear law developed by Camacho and Ortiz (1996). The distinction between these two approaches is associated with the way the damage initiation process is modeled. In the extrinsic case, the stress-based failure criterion is external to the cohesive element. When the tractions acting along the interface between two volumetric elements have reached a critical value, the interface is allowed to open in accordance with a prescribed traction–separation relation by introducing additional nodes, along the failed interface, coupled by a cohesive law. In the intrinsic approach, the failure criterion is incorporated within the constitutive model of the cohesive elements. Failure is integrated into the cohesive law by increasing the cohesive tractions from zero to a failure point at which the tractions reach a maximum before gradually decreasing back to zero values. Implementation of the intrinsic method in a finite element analysis requires that the cohesive elements be present between the volumetric elements from the beginning of the analysis, unlike the extrinsic approach, where a cohesive element is introduced in the mesh only after the corresponding interface is predicted to start failing. This adds some *artificial* flexibility to the solid, which could alter wave speeds and induce spreading of the wave. We will get back to this feature in relation to the bilinear cohesive law used in our model.

Other developments have also contributed to advances in the simulation of both quasi-static and dynamic fracture events. Theses include meshless methods (Belytschko et al., 1996, 2000; Belytschko and Tabbara, 1996), extended finite element methods, (Belytschko et al., 2001), atomistic modeling of fracture (Abraham et al., 1994, 1998; Gao, 1996; Gumbsch et al., 1997), and the avail-

ability of massively parallel computational environments necessary for complex dynamic failure problems. In the case of atomistic simulations, it should be noted that the development of algorithms for bridging length scales is needed and remains under intense investigation (Kohlhoff et al., 1991; Miller et al., 1998).

During the last few years, the mechanical behavior of polycrystalline ceramics has been studied quite extensively on a microstructural bases. This inevitably requires spanning multiple length scales. Instead of proceeding phenomenologically, the principles and tools of mechanics are brought to bear on phenomena occurring at the microscale. The observer then steps back and the microscopic features blur into macroscopic fields governed by a different set of "*effective*" laws. The determination of these effective properties from first principles is one of the principal objectives of micromechanics. A related endeavor is the use of the knowledge base thus acquired for the design of microstructures resulting in improved material properties.

The main characteristic of material microstructure models is the capability to include, in an explicit form, the heterogeneities of the material, such as grain shape, size and orientation, second phases, voids, flaws, etc. Some models include "ad hoc" finite elements to represent heterogeneities. For instance, Ghosh and Yunshan (1995) and Ghosh et al. (1997) developed a material based *Voronoi cell finite element model* (VCFEM) to study metal–matrix composites. Onck and Van der Giessen (1999) introduced the "*grain element*" where the grain boundaries account for viscous grain boundary sliding, and nucleation and growth of voids. Discrete propagation of the main crack occurred by linking up of neighboring facet microcracks.

Among the material microstructure models based on the standard finite element method, including cohesive interfaces, one can mention the work by Zhou and Zhai (1999) and Zhai and Zhou (2000), who analyzed the dynamic crack propagation in ceramic composites using the cohesive finite element model proposed by Needleman (1988) and Xu and Needleman (1995), and the work by Helms et al. (1999), where the cohesive interfaces were embedded along grain boundaries. Zavattieri and Espinosa (2001) simultaneously performed similar analysis applied to the modeling of microcracking of ceramics. Stochastic effects were included in these analyses and comparisons with experiments were performed.

Other methods based on a statistical approach, such as the model by Ostoja-Starzewki (1998) and Ostoja-Starzewki and Wang (1999) achieved bridging between micromechanical and continuum models where the microstructural material randomness is considered below the level of a single finite element. Likewise, Mullen et al. (1997) developed a finite element-based Monte Carlo that can be used to predict scatter in the nominal elastic constants and fracture of thin films. Wu and Niu (1995a,b) presented a micromechanical model of the fracture of polycrystalline ice. Their model is based on a statistical description of the ice microstructure, which contains crystals of random sizes and orientations, and a random distribution of grain boundary crack precursors.

Other models which include microcracking at the grain level can be found in the literature. Grah et al. (1996) conducted computer simulations of polycrystalline materials using a spring-network model for arbitrary in-plane crystal anisotropy. A detailed study of the interrelated physical mechanisms that result in failure modes in crystalline materials with high angle grain boundaries has been conducted by Zikry and Kao (1996). Kim et al. (1996) studied crack propagation in alumina ceramics. In their work, the competition between intergranular and transgranular propagation was utilized to determine the crack path.

Despite all these advances in the area of micromechanics, bridging between micro- and macroscales still remains one of the most challenging goals. Although in some instances comparison with experimental findings and microscopy studies have been done, the majority of the contributors omit comparison and correlation with experimental data. The accuracy of micromechanical models in capturing experimental data was assessed by Zavattieri and Espinosa (2002) and Zavattieri and Espinosa (2001). In order to provide a powerful tool in understanding the mechanisms that lead to macroscopic failure and to refine theories of damage utilized in continuum, or continuum/discrete

models, a grain level micromechanical model is presented in this paper to assess intergranular microcrack initiation and evolution. A representative volume element (RVE) of an actual microstructure, subjected to multi-axial dynamic loading, is considered for the different analyses. An elastic-anisotropic model for the grains, incorporating grain anisotropy by randomly generating principal material directions, is included. Cohesive interface elements are embedded along grain boundaries to simulate microcrack initiation and evolution. Their interaction and coalescence are a natural outcome of the calculated material response.

A variation of this micromechanical model for quasi-static calculations is also discussed in this paper for the simulation of cooling, and resulting thermal residual stresses, during the material fabrication process. Residual stresses due to mismatch between thermal expansion coefficients of adjacent grains and phases can result in spontaneous microcracking (Tvergaard and Hutchinson, 1988). An implicit incremental algorithm for modeling thermal effects is included together with the formulation of non-linear cohesive interfaces.

Our micromechanical model provides explicit account for arbitrary microstructural morphologies and microscopic fracture patterns making easier to identify and design microstructural configurations that enhance fracture toughness, and therefore lead to improve fabrication of new single and multi-layer ceramic materials. Through the consideration of actual microstructures, the effects of various fracture mechanisms is delineated. The unique advantages of the micromechanical model proposed in this work include: (1) explicit account of real, arbitrary material microstructures, (2) explicit modeling of fracture in a non-constrained manner, therefore arbitrary crack paths or microcrack patterns are admitted, (3) direct analysis of the stochastic nature of fracture in heterogeneous microstructures, (4) analysis of the effect of residual stresses, (5) resolution of fracture explicitly over multiple length scales and free of ad hoc fracture criterion, therefore crack initiation, growth, and coalescence is a natural outcome of material response, applied loading, and boundary constrains, (6) the representative computational cells where the calculations take place are chosen such that direct comparison with experimental data can be made.

2. Grain level micromechanical model

In this section, the micromechanical finite element modeling of ceramic microstructures under dynamic loading is presented to assess intergranular microcrack initiation and evolution. A RVE of a ceramic microstructure, subjected to multi-axial dynamic loading, is considered for the analysis. The model is based on a plane strain analysis of a polycrystalline material described with a multi-body finite element mesh. Each grain is individually represented by a mesh with six-noded triangular finite elements, generated using Delaunay triangulations, and four-noded interface elements inserted at the grain boundary. In order to accomplish this, the following procedure has been utilized: (i) generation of polycrystalline microstructures, (ii) transformation of the microstructure into a finite element mesh and (iii) time and space integration of governing differential equations.

2.1. Generation of the polycrystalline microstructure

The first step to provide an appropriate input to this micromechanical model is to obtain the geometry of the material microstructure. The grain geometry can be obtained from digitalization of an SEM micrograph or by means of geometrical algorithms. In this section the two methods are described.

2.1.1. Digitalization of micrographs

A real ceramic microstructure is digitized to represent the grain morphology as shown in Fig. 1. After digitalization, the grain boundaries are represented by polygons and a mesh is generated inside each polygon using Delaunay triangulation. Interface elements, along the grain facets, are added. The nodes belonging to the interface elements are the nodes of the triangular elements on the grain boundaries.

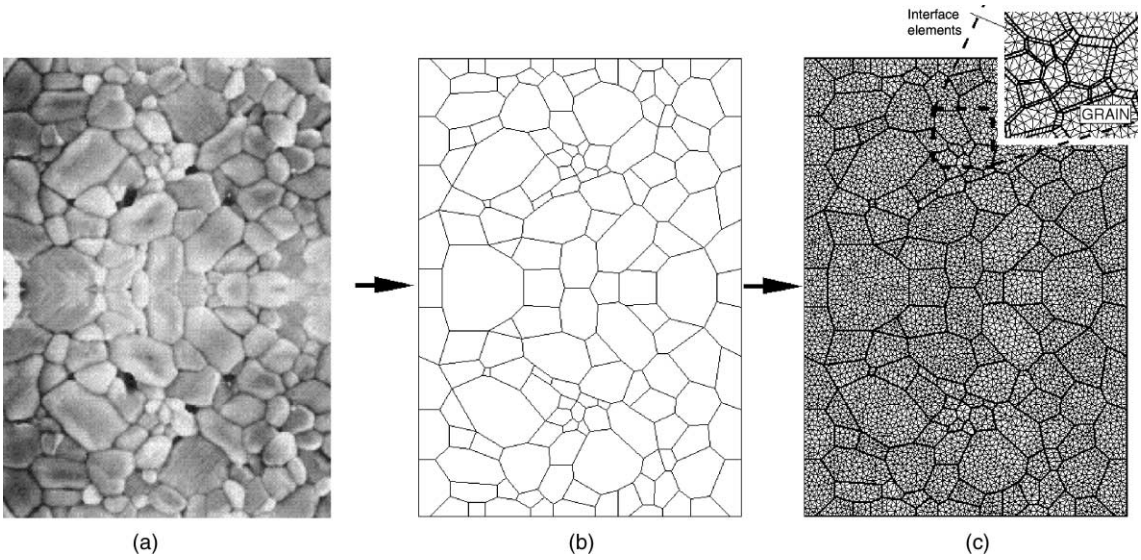

Fig. 1. RVE definition and mesh generation from digitalization of an actual microstructure.

2.1.2. Voronoi tessellations

It is well established that the grain structure in polycrystalline materials can be simulated by a Voronoi tessellation. Consider a pair of points, or nuclei, p and q located in the plane. The plane can be bisected into halves as follows; the mid-point of the line $\overline{pq}$ connecting p and q, and the slope of the line perpendicular to $\overline{pq}$ together define the bisector line that divides the plane in two halves, each of which contains the points that are closer to one of the dots. For the two-dimensional case, a plane is divided into $\mathscr{M}$ grain-like tiles (or polygons) corresponding to $\mathscr{M}$ nuclei that may be thought as nuclei of grains. A grain-like tile $\mathscr{T}_i$ is defined as follows: $\mathscr{T}_i = \{x : d(\mathbf{x}, \mathscr{P}_i) < d(\mathbf{x}, \mathscr{P}_j) \text{ for all } i \neq j\}$, where $\mathscr{P}_i$ represents a nucleus and $d(\mathbf{x}, \mathscr{P}_i)$ denotes the distance between $\mathscr{P}_i$ and $\mathbf{x}$. Fig. 2(a) shows an example for three tiles $\mathscr{T}_i$, $\mathscr{T}_j$ and $\mathscr{T}_k$. The set of complete tiles (polygons) is called the *Voronoi diagram*. Note that the nuclei that are closer to the borders of the area may not have sufficient numbers of neighbors to form a complete polygon. Such incomplete polygons and the Voronoi diagram define the *open Voronoi tessellation* of the entire plane (see Fig. 2). In order to get the *closed Voronoi tessellation* special care on the microstructure boundary has to be taken (see Fig. 2(c)). Each tile is named a Voronoi cell and represents an individual grain that is meshed using Delaunay triangulation (see Fig. 2(d)).

Several investigators have used this technique to represent polycrystalline materials. Ghosh and Yunshan (1995) and Ghosh et al. (1997) utilized Voronoi cells to obtain stereologic information for the different morphologies. In this approach each cell is an element in the VCFEM. Liu et al. (1998) proposed a method to investigate the damage evolution under uniaxial tension and reversed shear loading conditions, by means of a combined continuum damage and mechanism-based cavitation model, using a Voronoi tessellation to represent the polycrystal microstructure. Bolander and Saito (1998) used Voronoi tessellation to discretize homogeneous, isotropic materials prone to fracture such as cement and concrete. They modeled brittle fracture by means of a rigid-body-spring network.

In order to study the effect of grain morphology, Voronoi tessellations are utilized to generate different randomly shaped microstructures. A cloud of nuclei $\mathscr{P}_i$ is randomly generated with a uniform distribution along a specified region of the space (i.e., microstructure domain). Neighbor nuclei closer than a given tolerance are inhibited in order to limit the minimum grain size. After that, a

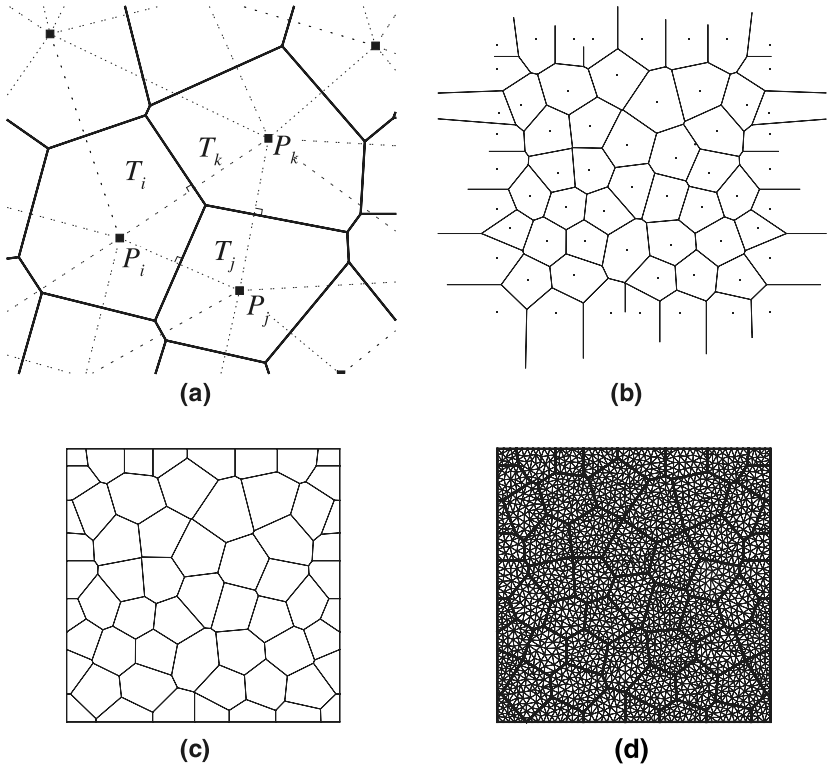

Fig. 2. (a) Schematics showing three tiles formed by three nuclei, (b) open Voronoi tessellation, (c) closed Voronoi tessellation, (d) finite element mesh.

Delaunay mesh generator is utilized to obtain the Voronoi tessellation associated with the nuclei $\mathscr{P}_i$. Grain size and shape are given by the number and distance between nuclei.

2.2. Discretized form of governing differential equation

The finite element analysis of the initial boundary value problem is performed using a total Lagrangian continuum approach with a large deformation elastic-anisotropic model. A displacement-based finite element formulation is obtained from the weak form of the momentum balance or dynamic principle of virtual work. The weak form at time t in total Lagrangian co-ordinates, (i.e., referred to the reference configuration), is given by

$$\int_{B_0} [\nabla_0 \mathbf{T}^0 + \rho_0(\mathbf{b}_0 - \mathbf{a})] \cdot \eta \, \mathrm{d}B_0 = 0 \tag{1}$$

$$\int_{B_0} \mathbf{T}^0 : \nabla_0 \eta \, \mathrm{d}B_0 - \int_{B_0} \rho_0(\mathbf{b}_0 - \mathbf{a}) \cdot \eta \, \mathrm{d}B_0 - \int_{S_{0\sigma}} \mathbf{t} \cdot \eta \, \mathrm{d}S_0 = 0 \tag{2}$$

where $\mathbf{T}^0$ is the first Piola–Kirchoff stress tensor at time t; $\mathbf{b}_0$, $\mathbf{a}$, and $\mathbf{t}$ are the body force vector, acceleration vector, and boundary traction vector on volume B_0 and boundary $S_{0\sigma}$, respectively. Virtual displacement field η is assumed to be admissible, and ρ_0 represents the material density per unit volume in the reference configuration. The symbol ∇_0 denotes the material gradient with respect to the reference configuration, and ':' is used to denote the inner product between second order tensors, e.g., $\mathbf{A} : \mathbf{B} \equiv A_{ij}B_{ji}$, where the summation convention on repeated indices is implied.

Alternately, the weak form of the momentum balance, in terms of spatial quantities, is given by

$$\int_{B_0} \tau : \nabla^{s}\eta \, \mathrm{d}B_0 - \int_{B_0} \rho_0(\mathbf{b}_0 - \mathbf{a}) \cdot \eta \, \mathrm{d}B_0 - \int_{S_{0\sigma}} \mathbf{t} \cdot \eta \, \mathrm{d}S_0 = 0 \tag{3}$$

in which superscript s stands for the symmetric part of the tensor, $\tau = \mathbf{F}\mathbf{T}^0$ is the Kirchoff stress, $\mathbf{F}$ is the deformation gradient at time t, and ∇ is the spatial deformation tensor. As Eq. (3) shows, the equation of motion in its weak form states that the work done by the stresses τ over strains $\nabla^{s}\eta$ equals the work done by applied body forces, inertia forces, and surface tractions.

In the absence of body forces, substitution of the discretized variables into Eq. (3) leads to the following system of ordinary differential equations. The above equation can be written at time t for explicit integration as,

$$\mathbf{M}\mathbf{a} = \mathbf{f}_{\text{ext}} - \mathbf{f}_{\text{int}} \tag{4}$$

where $\mathbf{M}$ is the lumped mass matrix, $\mathbf{a}$ is the global acceleration vector and $\mathbf{f}_{\text{ext}}$ and $\mathbf{f}_{\text{int}}$ are the external and internal force vectors. In order to obtain a uniform mass distribution in the mesh, the element mass was lumped proportionally to the angles formed by the corner nodes and mid-nodes, as detailed by Espinosa et al. (1998b).

2.2.1. Anisotropic elastic model

An elastic-anisotropic model is used to describe the grains single crystal behavior. The second Piola–Kirchoff stress tensor relative to the undeformed configuration is described by

$$\mathbf{S}_{ij} = \mathscr{C}_{ijkl}\mathbf{H}_{kl} \tag{5}$$

where $\mathbf{H} = (1/2)\ln\mathbf{C}$ is a logarithmic strain measure or Henky strain, $\mathbf{C} = \mathbf{F}\mathbf{F}^T$ is the elastic right Cauchy–Green deformation tensor, and $\mathscr{C}_{ijkl}$ is the elastic anisotropic material stiffness tensor in the global co-ordinates (x, y, z).

In the case of anisotropic crystals, the elastic constitutive matrix $\widehat{\mathscr{C}}_{IJKL}$ is defined in the local co-ordinate system of the grain by its principal material directions $(1, 2, 3)$, such that $\mathscr{C}_{ijkl} = \mathbf{T}^c_{iI}\mathbf{T}^c_{jJ}\mathbf{T}^c_{kK}\mathbf{T}^c_{lL}\widehat{\mathscr{C}}_{IJKL}$, where $\mathbf{T}^c$ is the transformation matrix.

Each grain is assumed to be elastic orthotropic and the orientation of the principal material directions differs from grain to grain. In order to keep the plane strain condition in the x–y plane, one of the principal material directions has to coincide with the z-axis. Therefore, three cases are considered randomly for each grain, Case 1: $1 \equiv z$, Case 2: $2 \equiv z$ or Case 3: $3 \equiv z$. The angle between the global axes x, y, and the two local axes lying in the plane x–y is also generated randomly. The grain local axes and the corresponding analysis global axes are shown in Fig. 3. In general, this approach could be used for any orthotropic materials where the normal to the three symmetry planes coincides with the local axes of co-ordinates, i.e., tetragonal systems: *indium*, *tin*, *zircon*; transversely isotropic systems: *cadmium*, *ice*, *zinc*; cubic systems: *aluminum*, *copper*, *nickel*, etc.

3. Cohesive model: contact/interface algorithm

A multi-body contact–interface algorithm to describe the kinematics at the grain boundaries is used to simulate crack initiation and propagation. An explicit time integration scheme is adapted to integrate the system of spatially discretized ordinary differential equations. Fig. 4 describes the contact model, which is integrated with interface elements to simulate microcracking at the grain boundaries and subsequent large sliding, opening and closing of the interface. The tensile and shear tractions in the zero thickness interface elements, embedded along grain boundaries, are calculated from the interface cohesive law.

The interface cohesive law describes the evolution of these tractions in terms of both normal and tangential displacement jumps. Within the framework of cohesive interface elements, the two most noteworthy cohesive failure models available in the literature are the potential-based law used by Tvergaard (1990) and Xu and Needleman (1995), and the linear law developed by Camacho and Ortiz (1996) and Ortiz and Pandolfi (1999).

Our model assumes that the interface carries forces that oppose separation and shear between two surfaces until debonding. The magnitude of these forces is a function of the relative separation and shear displacements between the two surfaces. The compressive tractions at the grain boundaries

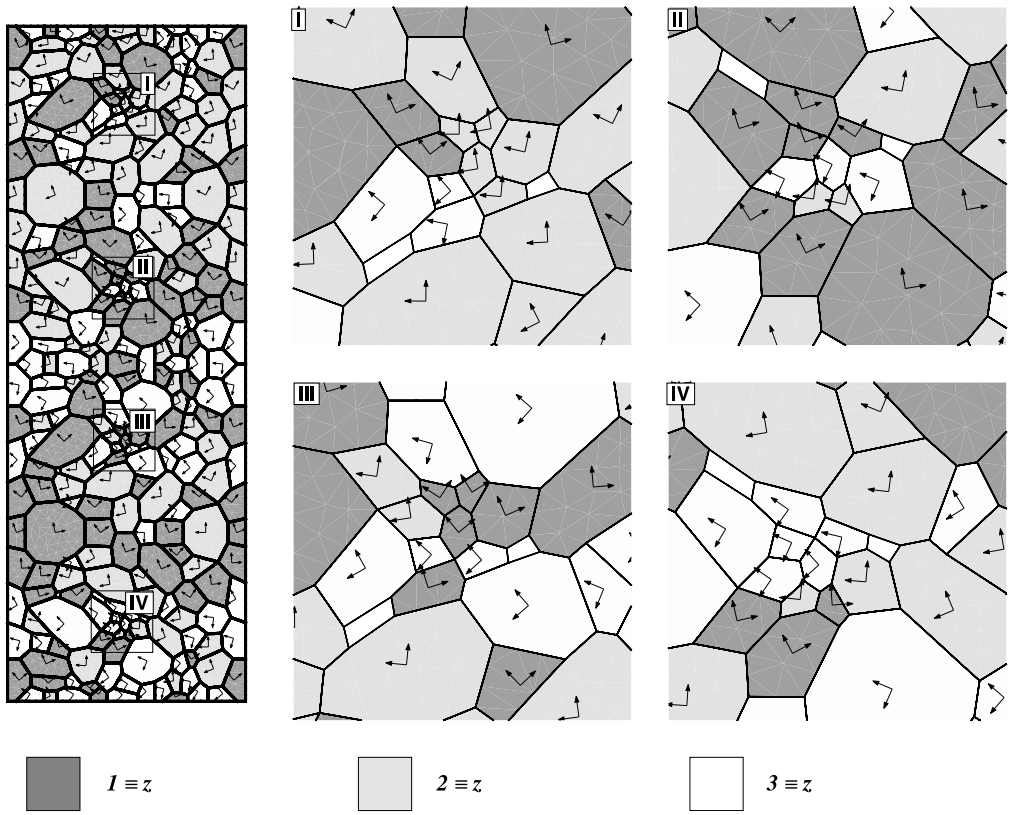

Fig. 3. Distribution of principal material directions within each grain. Different intensities of gray indicate which principal direction coincides with the global z-axis. The local system of co-ordinates in the x–y plane is represented by two vectors.

are calculated through the impenetrability condition employed in the contact model. The interface between two bodies is intact until the interface traction reaches the maximum value. Once the maximum traction is reached, the interface starts deteriorating and the traction reduces to zero linearly up to the maximum displacement jump.

Once the effective displacement jump reaches or exceeds a value of 1, the interface element is assumed to have failed and microcracking is said to have initiated at that grain boundary. Subsequent failure of neighboring interface elements leads to microcrack propagation and coalescence. In our graphic representation, failed interface elements are represented with thicker lines (see Fig. 4).

The description for the formulation of the interface element presented here is based on the zero thickness four-noded linear interface element, but it can be easily extended for six-noded quadrilateral interface elements (Dwivedi and Espinosa, 2003). Fig. 5 shows an schematics of the four-noded linear interface element and the six-noded quadrilateral interface element.

The four-noded elements are inserted between volumetric elements such that nodes 1 and 2 belong to one fragment and nodes 3 and 4 to the other. The displacement jumps are defined at the mid-plane of the element. Hence, the shape factors of the element are also given on its mid-plane as if it was a two-noded linear element, i.e., $N_1 = (1-\eta)/2$ and $N_2 = (1+\eta)/2$. In essence, this makes the element similar to a four-noded quadrilateral differential element. Given the inclination of the element with the global X-axis, the normal and tangential displacements in the plane of the element can be obtained from the global displace-

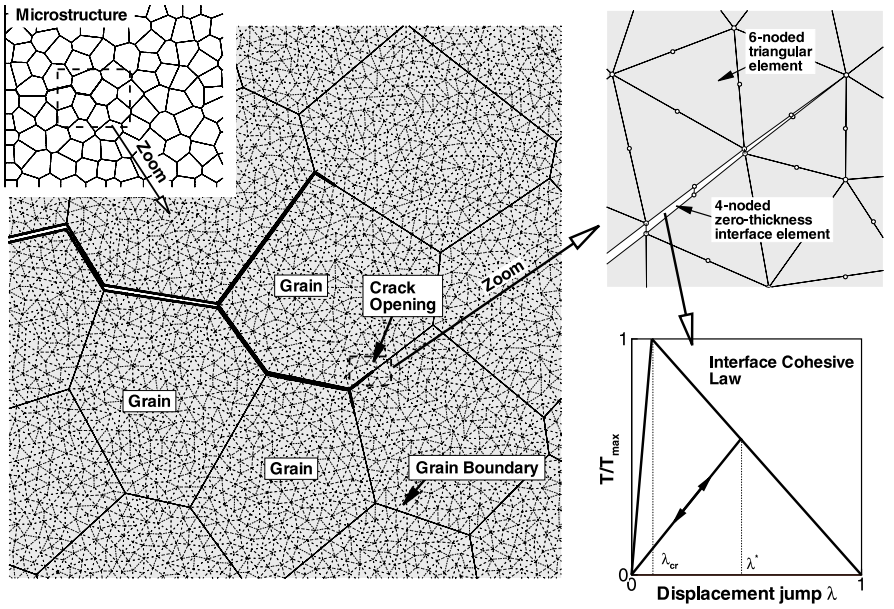

Fig. 4. Schematics of microcracking at grain boundaries using an irreversible interface cohesive law. Also shown is the evolution of the traction vector magnitude in loading and unloading.

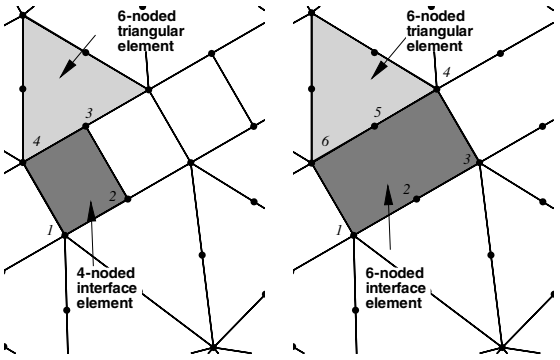

Fig. 5. Schematics of a four-noded linear interface element and a six-noded quadratic interface element.

ments at each node. Then the normal and tangential displacement jumps at the interface can then be obtained by the difference between the normal and tangential nodal displacements as described by Dwivedi and Espinosa (2003) and Emore (1996).

The normal tensile and shear traction at the interface are determined from the interface cohesive law. The nodal forces in the plane of the element are computed from the known interface traction as;

$$F' = \int_{S'} N_s^T \mathbf{T}\, \mathrm{d}S' \tag{6}$$

where F' is the force vector (F_t, F_n), $\mathbf{T}$ is the computed interface traction vector (T_t, T_n) and N_s is the shape function vector, all quantities are defined in the local co-ordinates of the element. The integration of the above equation is carried out using a two points quadrature rule. The computed forces are then transformed to the global co-ordinates as, $F = T_g F'$, where T_g is the transformation matrix. The forces so obtained at the mid-plane of the element are applied to nodes 1 and 2 and equal and opposite forces are applied to nodes 3 and 4. These normal and tangential tractions contribute to the internal nodal forces so that the f_{ia}^{inte} becomes;

$$\begin{aligned} f_{ia}^{\text{inte}} &= \sum_e \int_{B_0^e} \mathbf{B}^T \tau\, \mathrm{d}B_0 + f_{ia}^{\text{inte}} \\ &= \sum_e \int_{B_0^e} \mathbf{B}^T \tau\, \mathrm{d}B_0 + \sum_{\text{inte}} \int_{S_e^{\text{inte}}} T_g \mathbf{N}_s^T \mathbf{T}\, \mathrm{d}S \end{aligned} \tag{7}$$

where f_{ia}^{inte} is the force contributed by interface element to node i, which is calculated by integrating the interface tractions over the mid-surface of the element. The three cohesive laws used in the analyses are given as follows:

3.1. Law I

In formulating the cohesive law, a non-dimensional effective displacement jump is defined by

$$\lambda = \sqrt{\left(\frac{u_{\text{n}}}{\delta_{\text{n}}}\right)^2 + \left(\frac{u_{\text{t}}}{\delta_{\text{t}}}\right)^2} \tag{8}$$

where, u_{n} and u_{t} are the actual normal and tangential displacement jumps at the interface estimated by the finite element analysis, and δ_{n} and δ_{t} are critical values at which interface failure takes place.

In this first law, based on Tvergaard (1990), the equivalent τ, normal traction T_{n} and tangential traction T_{t} evolve quadratically with the effective displacement jump as:

$$\tau(\lambda) = \tfrac{27}{48} T_{\max}(1 - 2\lambda + \lambda^2) \tag{9}$$

$$\begin{aligned} T_{\text{n}} &= \frac{u_{\text{n}}}{\delta_{\text{n}}}\tau(\lambda) \\ T_{\text{t}} &= \alpha\frac{u_{\text{t}}}{\delta_{\text{t}}} \end{aligned} \tag{10}$$

where $T_{\max}$ is the maximum normal traction that the interface can bear before failure and α is the parameter coupling normal and shear tractions.

The reversible and irreversible unloading is implemented by taking λ_{cr}, which is the same as the value of λ at which the traction are maximum, i.e., $\lambda_{\text{cr}} = 1/3$. Accordingly, the normal and tangential traction are given as:

For loading and unloading in the range $0 \leqslant \lambda \leqslant \lambda_{\text{cr}}$

$$\begin{aligned} T_{\text{n}} &= \frac{u_{\text{n}}}{\delta_{\text{n}}}\tau(\lambda) \\ T_{\text{t}} &= \alpha\frac{u_{\text{t}}}{\delta_{\text{t}}}\tau(\lambda) \end{aligned} \tag{11}$$

For loading in the range $\lambda_{\text{cr}} \leqslant \lambda \leqslant 1$, or, $\lambda_{\text{u}} \leqslant \lambda \leqslant 1$, where λ_{u} is the value of λ from where the last unloading had taken place,

$$\begin{aligned} T_{\text{n}} &= \frac{u_{\text{n}}}{\delta_{\text{n}}}\tau(\lambda) \\ T_{\text{t}} &= \alpha\frac{u_{\text{t}}}{\delta_{\text{t}}}\tau(\lambda) \end{aligned} \tag{12}$$

And lastly, for unloading and reloading in the range $0 \leqslant \lambda \leqslant \lambda_{\text{u}}$

$$\begin{aligned} T_{\text{n}} &= \frac{u_{\text{n}}}{\delta_{\text{n}}}\tau(\lambda_{\text{u}})\frac{\lambda}{\lambda_{\text{u}}} \\ T_{\text{t}} &= \alpha\frac{u_{\text{t}}}{\delta_{\text{t}}}\tau(\lambda_{\text{u}})\frac{\lambda}{\lambda_{\text{u}}} \end{aligned} \tag{13}$$

Fig. 6 shows normal and tangential components of the cohesive traction as a function of normal and tangential displacements. Fig. 7(a) shows the variation of normal traction as a function of the normal displacement and how it is affected by the contribution of a tangential displacement. A similar plot is shown for the tangential traction versus the tangential displacement in Fig. 7(b). The area under the normal traction–normal displacement jump curve, in the absence of a tangential displacement jump, gives the critical strain energy release rate G_{Ic}. Similarly, the area under the tangential traction–tangential displacement jump curve, in the absence of a normal displacement jump, gives the critical strain energy release rate G_{IIc}. The law yields G_{Ic} and G_{IIc} as,

$$G_{\text{Ic}} = \tfrac{27}{48} T_{\max}\delta_{\text{n}}; \quad G_{\text{IIc}} = \tfrac{27}{48}\alpha T_{\max}\delta_{\text{t}} \tag{14}$$

A physical meaning for parameter α then follows as:

$$\alpha = \frac{G_{\text{IIc}}}{G_{\text{Ic}}}\left(\frac{\delta_{\text{n}}}{\delta_{\text{t}}}\right) \tag{15}$$

Fig. 8 shows loading and unloading paths after irreversible failure.

When $\lambda \geqslant \lambda_{\text{cr}}$ the critical strain energy release rate decreases to G_{Ic}^{c}, then G_{dis} is the dissipated energy due to the irreversibility,

$$G_{\text{dis}}(\lambda_{\text{u}}) = G_{\text{Ic}} - G_{\text{Ic}}^{c} = \tfrac{27}{48} T_{\max}\delta_{\text{n}}(2\lambda_{\text{u}}^2 - \lambda_{\text{u}}^4) \tag{16}$$

and the percentage of dissipated energy is:

$$\frac{G_{\text{dis}}}{G_{\text{Ic}}} = 2\lambda_{\text{u}}^2 - \lambda_{\text{u}}^4 \tag{17}$$

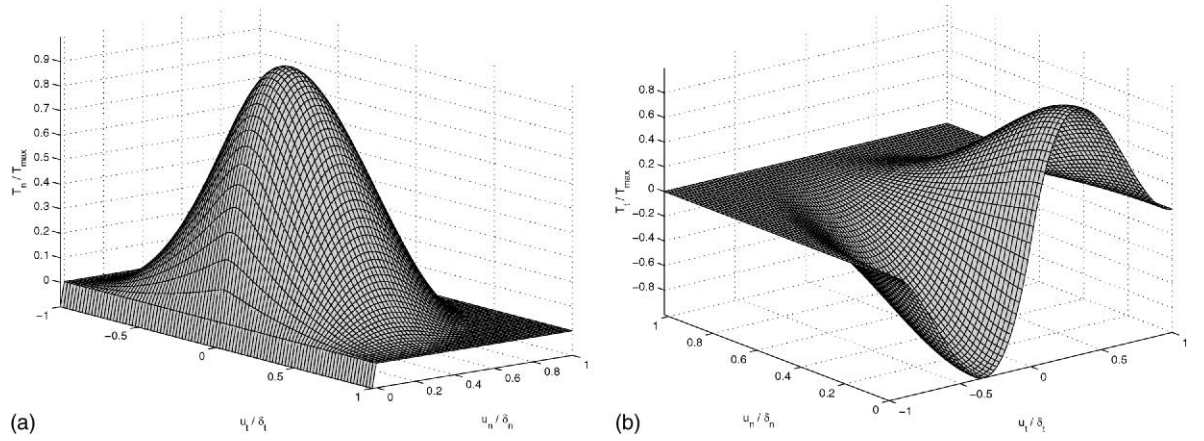

Fig. 6. Cohesive law I: (a) Variation of normal cohesive traction T_n/T_{max}. (b) Variation of shear cohesive traction T_t/T_{max}.

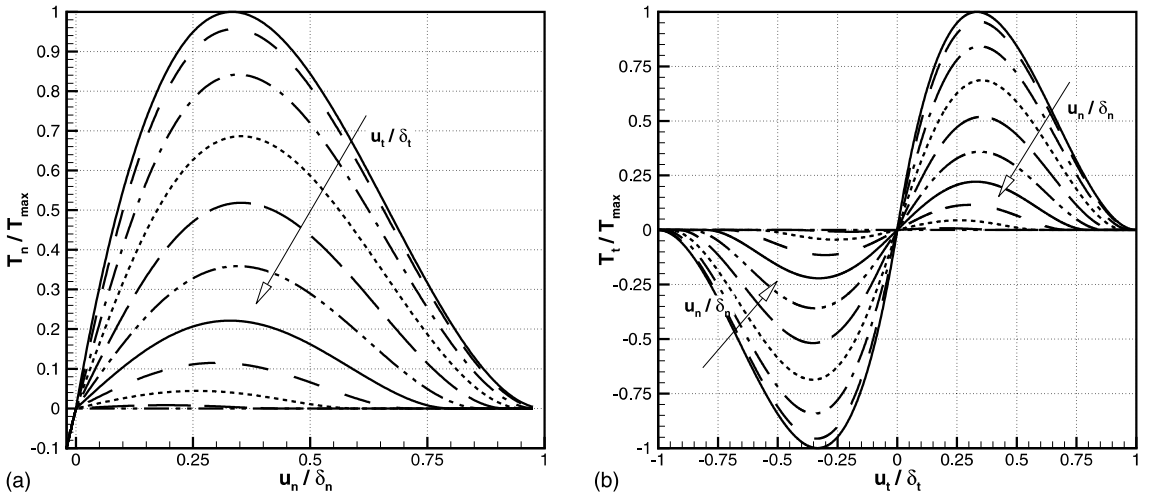

Fig. 7. Cohesive law I: (a) Variation of the tensile cohesive traction T_n/T_{max} as a function of u_n/δ_n for different values of u_t/δ_t. (b) Variation of shear cohesive traction T_t/T_{max} as a function of u_t/δ_t for different values of u_n/δ_n.

3.2. Law II

Since in the Tvergaard τ–δ law, the initial interface stiffness is fixed, an alternative cohesive law is formulated in which a critical displacement jump λ_{cr}, at which $T = T_{max}$ defines a reversible regime. In formulating this second cohesive law, a non-dimensional effective displacement jump is defined as

$$\lambda = \sqrt{\left(\frac{u_n}{\delta_n}\right)^2 + \xi^2\left(\frac{u_t}{\delta_t}\right)^2} \tag{18}$$

where, u_n and u_t are the current normal and tangential displacement jumps at the interface estimated by the finite element analysis, and δ_n and δ_t are critical values at which interface failure takes place. This definition of the displacement jump was first proposed by Ortiz and Pandolfi (1999).

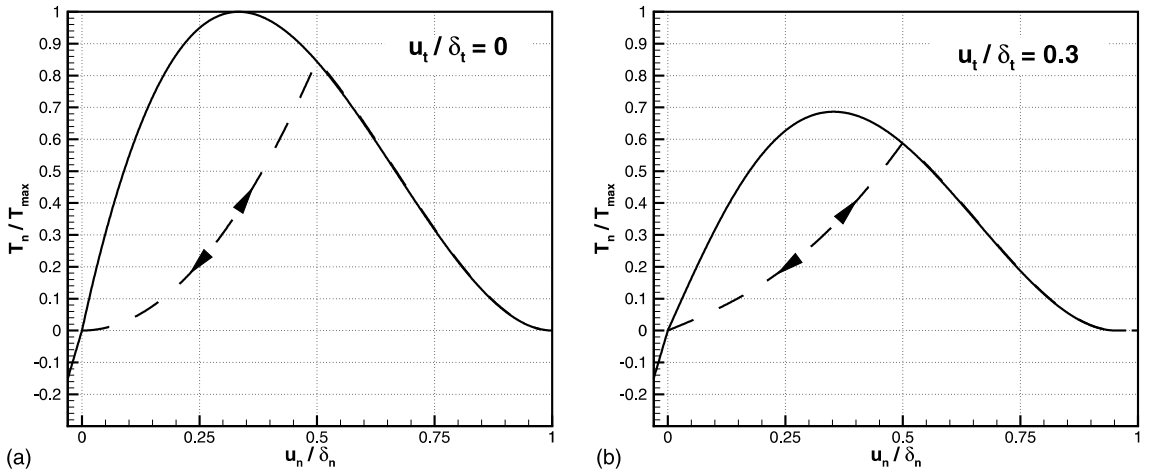

Fig. 8. Irreversible loading and unloading beyond λ_{cr} for the cohesive law I.

Assuming a potential of the form

$$\Phi(u_n, u_t) = \delta_n \int_0^{\lambda} \sigma(\lambda')\, d\lambda' \tag{19}$$

and letting $\sigma(\lambda)$ be of the form

$$\sigma(\lambda) = \frac{(1-\lambda)}{(1-\lambda_{cr})} T_{max} \tag{20}$$

then Φ takes the form:

$$\Phi(u_n, u_t) = (2-\lambda^2)\frac{\delta_n}{2}\frac{T_{max}}{1-\lambda_{cr}} \tag{21}$$

The normal and tangential components of the traction acting on the interface in the fracture process zone are given by

$$T_n = \frac{\partial \Phi}{\partial u_n} = \frac{\partial \Phi}{\partial \lambda}\frac{\partial \lambda}{\partial u_n} = \frac{\sigma(\lambda)}{\lambda}\frac{u_n}{\delta n} \tag{22}$$

$$T_t = \frac{\partial \Phi}{\partial u_t} = \frac{\partial \Phi}{\partial \lambda}\frac{\partial \lambda}{\partial u_t} = \xi^2\left(\frac{\delta_n}{\delta_t}\right)\frac{\sigma(\lambda)}{\lambda}\frac{u_t}{\delta_t} \tag{23}$$

In this way the traction–separation law takes the form:

$$T_n = \frac{1-\lambda^*}{\lambda^*}\left(\frac{u_n}{\delta_n}\right)\frac{T_{max}}{(1-\lambda_{cr})} \tag{24}$$

$$T_t = \frac{1-\lambda^*}{\lambda^*}\left(\frac{u_t}{\delta_t}\right)\frac{\alpha T_{max}}{(1-\lambda_{cr})} \tag{25}$$

where $\alpha = \xi^2(\delta_n/\delta_t)$ and λ^* is monotonically increasing and given by:

$$\lambda^* = \max(\lambda_{max}, \lambda) \tag{26}$$

where $\lambda_{max} = \lambda_{cr}$ initially and $\lambda_{max} = \lambda$ if $\lambda > \lambda_{max}$.

Fig. 9 shows the variation of the tensile cohesive traction T_n/T_{max}, with respect to the non-dimensional normal and tangential displacement discontinuities u_n/δ_n and u_t/δ_t. Fig. 10 shows the variation of T_n as a function of u_n/δ_n for different values of u_t/δ_t and T_t as a function of u_t/δ_t for different values of u_n/δ_n.

Beyond λ_{cr}, the traction reduces to zero when $\lambda = 1.0$ and any unloading takes place irreversibly. The advantage of this formulation is that the irreversible behavior is already incorporated in the law. Since λ is defined by λ_{max}, the law ensures that λ^* remains constant for any unloading below λ_{max}. Fig. 11 shows the loading and unloading after irreversible failure.

From the values of fracture toughness K_{IC}, or equivalently G_{IC}, assuming plane strain, and the maximum interface stress, the critical interface displacement jump is computed by equating the area under the T_n–u_n diagram to G_{IC}, namely,

$$G_{Ic} = \tfrac{1}{2}\delta_n T_{max} \tag{27}$$

Similarly, the area under the curve tangential traction–tangential displacement jump, T_t–u_t, in

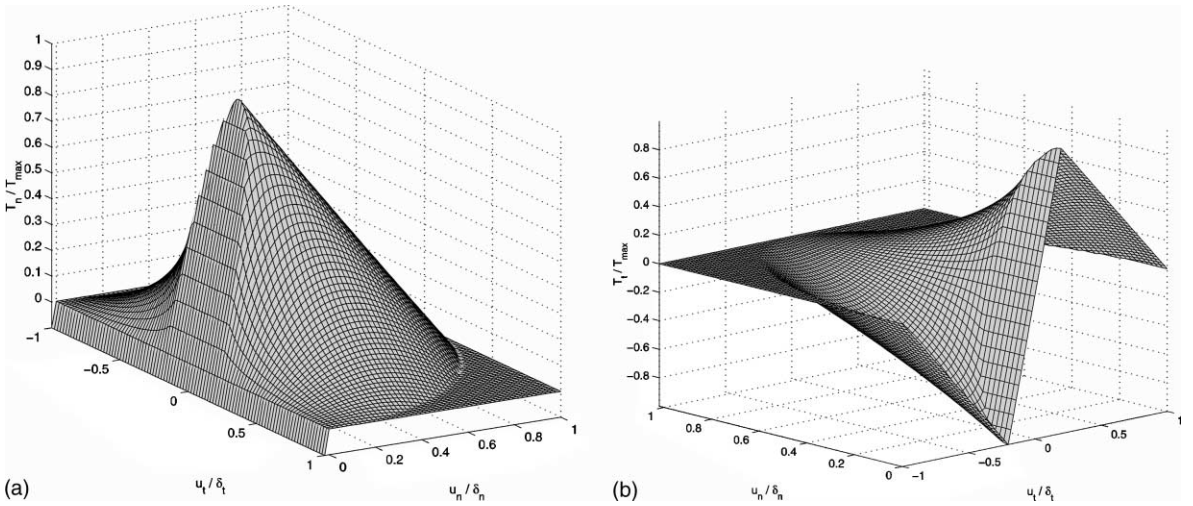

Fig. 9. Cohesive law II: (a) Variation of normal cohesive traction T_n/T_{max}. (b) Variation of shear cohesive traction T_t/T_{max}.

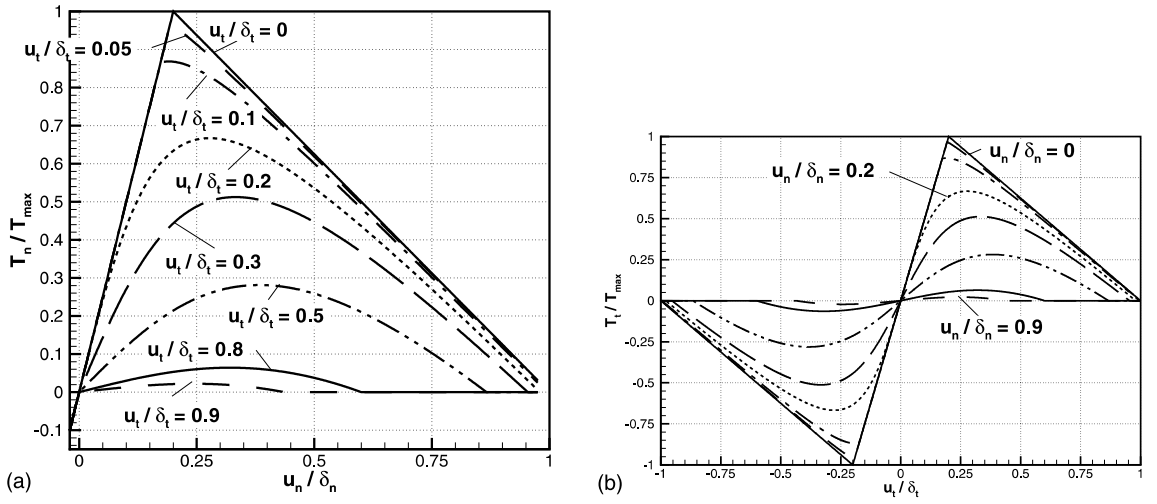

Fig. 10. Cohesive law II: (a) Variation of the tensile cohesive traction T_n/T_{max} as a function of u_n/δ_n for different values of u_t/δ_t. (b) Variation of shear cohesive traction T_t/T_{max} as a function of u_t/δ_t for different values of u_n/δ_n.

the absence of normal traction, gives the critical strain energy release rate G_{IIc}, viz.,

$$G_{IIc} = \frac{1}{2}\delta_t \alpha T_{max} = \xi^2 \frac{1}{2}\left(\frac{\delta_n}{\delta_t}\right)\delta_t T_{max} = \xi^2 G_{Ic} \qquad (28)$$

therefore,

$$\frac{G_{IIc}}{G_{Ic}} = \xi^2$$

which provides a physical meaning for ξ.

After $\lambda_{max} \geqslant \lambda_{cr}$, the critical strain energy release rate decreases to G_{Ic}^c, then the dissipated energy due to the irreversibility, G_{dis}, is given by

$$G_{dis}(\lambda_{max}) = G_{Ic} - G_{Ic}^c = \frac{1}{2}\delta_n T_{max}\left(\frac{\lambda_{max} - \lambda_{cr}}{1 - \lambda_{cr}}\right) \qquad (29)$$

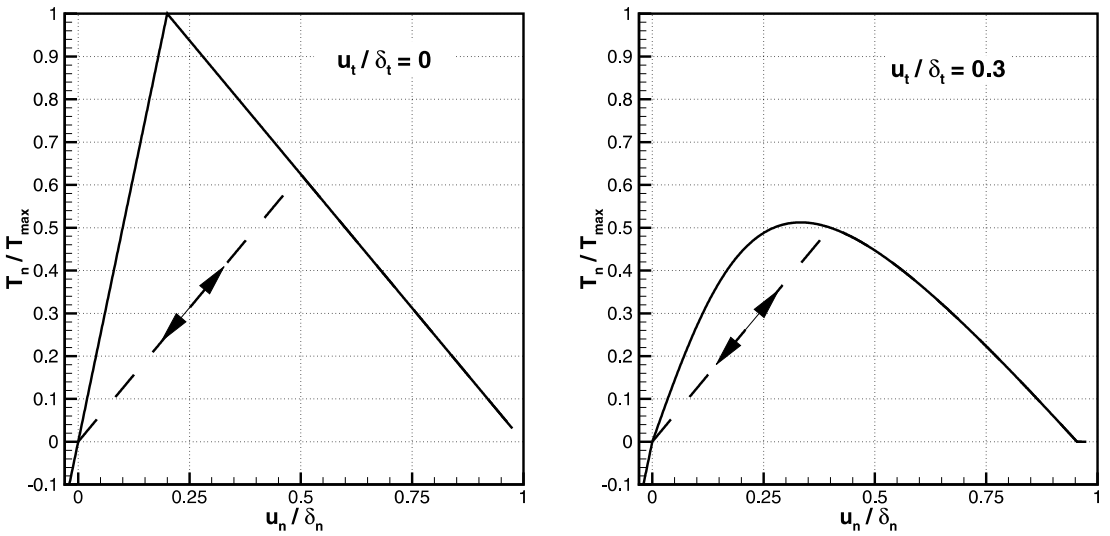

Fig. 11. Irreversible unloading beyond λ_{max} for cohesive law II.

And the percentage of dissipated energy is:

$$\frac{G_{dis}}{G_{Ic}} = \frac{\lambda_{max} - \lambda_{cr}}{1 - \lambda_{cr}} \tag{30}$$

3.3. Law III

There are instances in which the interface traction exhibits a plateau. This cohesive law is formulated to capture such interface behavior. In formulating this cohesive law, a non-dimensional effective displacement jump is defined by

$$\lambda = \sqrt{\left(\frac{u_n}{\delta_n}\right)^2 + \xi^2 \left(\frac{u_t}{\delta_t}\right)^2} \tag{31}$$

where u_n and u_t are the current normal and tangential displacement jumps at the interface estimated by the finite element analysis, and δ_n and δ_t are critical values at which interface failure takes place.

The traction–separation law is defined by

$$T_n = \xi \frac{(u_n/\delta_n)}{\lambda^*} T_{max} + (1-\xi)\frac{(1-\lambda^*)}{(1-\lambda_f)} \frac{\sqrt{\lambda_f^2 - \xi^2 (u_t/\delta_t)^2}}{\lambda_f} T_{max}$$

$$T_t = \xi \frac{(u_t/\delta_t)}{\lambda^*} \alpha T_{max} + (1-\xi)\frac{(1-\lambda^*)}{(1-\lambda_f)} \frac{\sqrt{\lambda_f^2 - (u_n/\delta_n)^2}}{\xi \lambda_f} \alpha T_{max} \tag{32}$$

In this law the end of the traction plateau is defined by a particular value of the effective displacement jump defined as λ_f. λ is monotonically increasing and it has the form:

$$\lambda^* = \max(\lambda_{max}, \lambda)$$

where $\lambda_{max} = \lambda_{cr}$ initially and $\lambda_{max} = \lambda$ if $\lambda > \lambda_{max}$. Therefore,

$$\lambda_f = \max(\lambda_f, \lambda_{max})$$

and

$$\xi = \begin{cases} 1 & \lambda < \lambda_f \\ 0 & \lambda \geqslant \lambda_f \end{cases}$$

For irreversible unloading when $\lambda > \lambda_{cr}$

$$\begin{aligned} &\text{if } \Delta u_n < 0 \quad \text{then } T_{max} = \frac{\lambda_{max}^c}{(u_n/\delta_n)^c} T_n^c \\ &\text{if } \Delta u_t < 0 \quad \text{then } T_{max} = \frac{\lambda_{max}^c}{\alpha (u_t/\delta_t)^c} T_t^c \end{aligned} \tag{33}$$

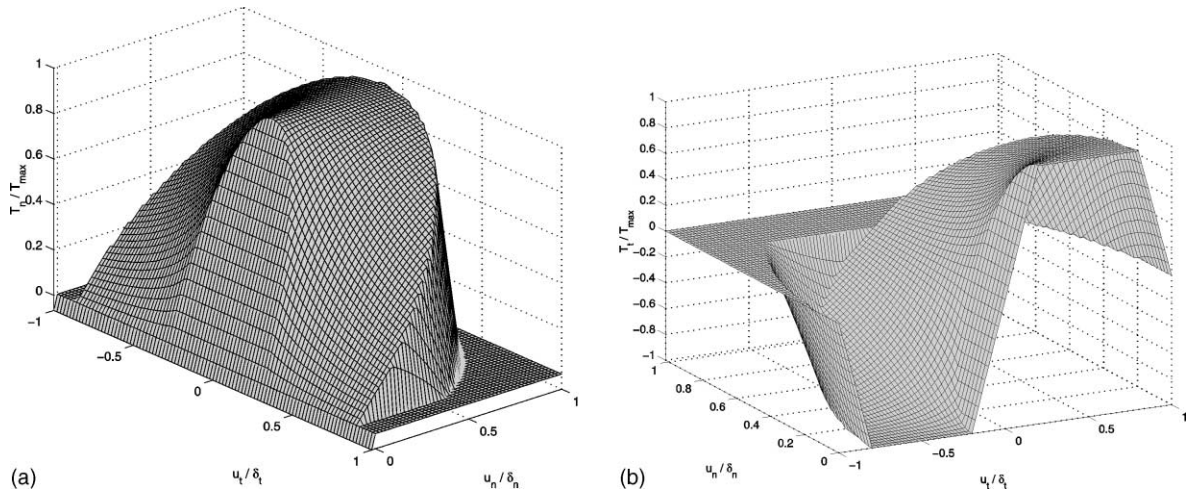

Fig. 12. Cohesive law III: (a) Variation of the tensile cohesive traction T_n/T_{max}. (b) Variation of shear cohesive traction T_t/T_{max}.

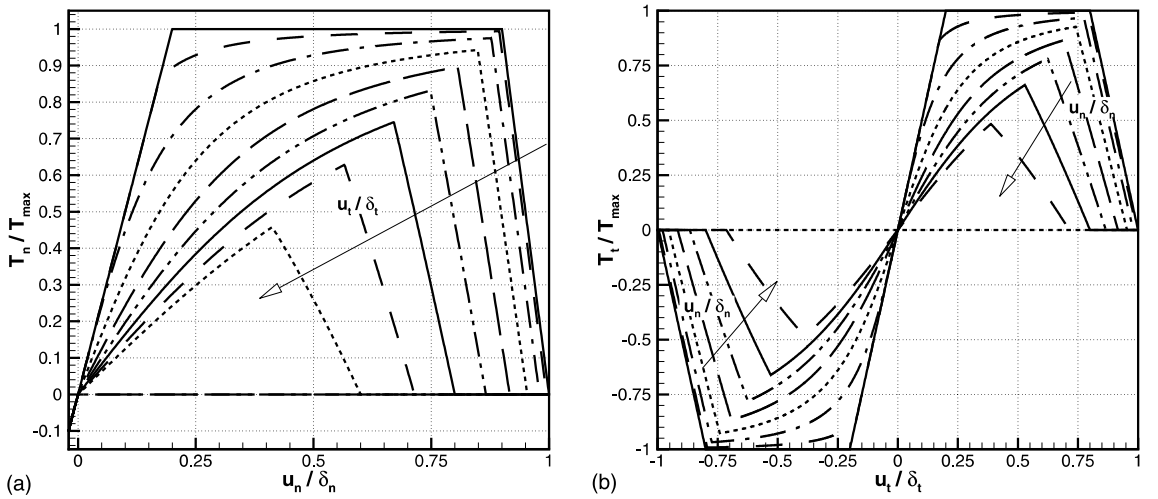

Fig. 13. Cohesive law III: (a) Variation of the normal cohesive traction T_n/T_{max} as a function of u_n/δ_n for different values of u_t/δ_t. (b) Variation of the shear cohesive traction T_t/T_{max} as a function of u_t/δ_t for different values of u_n/δ_n.

Fig. 12 shows the variation of the tensile cohesive traction T_n/T_{max}, with respect to the non-dimensional normal and tangential displacement discontinuities u_n/δ_n and u_t/δ_t. Fig. 13 shows the variation of T_n as a function of u_n/δ_n for different values of u_t/δ_t and T_t as a function of u_t/δ_t for different values of u_n/δ_n. Fig. 14 shows the loading and unloading after irreversible failure.

The area under the normal traction–normal displacement jump curve, in the absence of tangential traction, gives the critical strain energy release rate G_{Ic}. Similarly, the area under the tangential traction–tangential displacement jump curve, in the absence of normal traction, gives the critical strain energy release rate G_{IIc}. The law yields G_{Ic} and G_{IIc} as,

$$G_{Ic} = \tfrac{1}{2}\delta_n T_{max}(1 + \lambda_f - \lambda_{cr})$$
$$G_{IIc} = \tfrac{1}{2}\alpha\delta_t T_{max}(1 + \lambda_f - \lambda_{cr}) \quad (34)$$

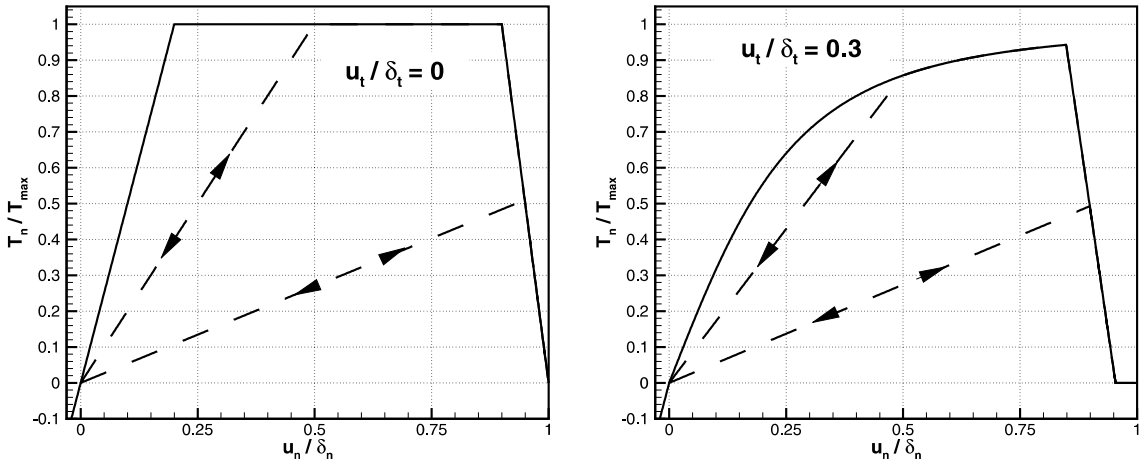

Fig. 14. Irreversible unloading beyond λ_{max} for cohesive law III.

For $\lambda_{cr} \leqslant \lambda_{max} < \lambda_f$ the critical strain energy release rate decreases to G_{Ic}^c, then the dissipated energy due to the irreversibility, G_{dis}, is:

$$G_{dis}(\lambda_{max}) = G_{Ic} - G_{Ic}^c = \tfrac{1}{2}\delta_n T_{max}(\lambda_{max} - \lambda_{cr}) \quad (35)$$

and the percentage of dissipated energy is:

$$\frac{G_{dis}}{G_{Ic}} = \frac{\lambda_{max} - \lambda_{cr}}{1 + \lambda_f - \lambda_{cr}} \quad (36)$$

Likewise, for $\lambda_f \leqslant \lambda_{max} \leqslant 1$ the critical strain energy release rate decreases to G_{Ic}^c, then the dissipated energy due to the irreversibility, G_{dis}, is:

$$G_{dis}(\lambda_{max}) = G_{Ic} - G_{Ic}^c = \frac{1}{2}\delta_n\left(T_{max} - T_n^c \frac{\lambda_{max}^c}{(u_n/\delta_n)^c}\right) \quad (37)$$

and the percentage of dissipated energy becomes:

$$\frac{G_{dis}}{G_{Ic}} = 1 - \frac{T_n^c}{T_{max}} \frac{\lambda_{max}^c}{(u_n/\delta_n)^c} \quad (38)$$

Other laws can be used, for instance the cohesive law proposed by Xu and Needleman (1994, 1995), Camacho and Ortiz (1996), Ortiz and Pandolfi (1999), Geubelle and Baylor (1998), etc. However, care must be exercised in selecting the initial stiffness of the cohesive law. In fact, for zero thickness cohesive laws, the addition of elements between regular elements adds an artificial flexibility that can result in modification of wave speeds in the material or penetrability of elements in compression. Cohesive laws such as the one proposed by Needleman may result in overlapping between fragments because the tractions are a function of the normal and tangential relative displacement, which makes the compression part softer, as the normal traction has contributions from the tangential displacement.

3.4. Some computational aspects of the cohesive model

3.4.1. Initial slope

As previously mentioned, the initial slope of the cohesive law must be selected with care. The slope of the function, in the range $0 < \lambda < \lambda_{cr}$, is selected such that the wave speed in the material is not affected by the interface elements.

In 1D, the traction–separation relation T–u for law II (Section 3.2) is given by

$$\begin{cases} T = \left(\dfrac{u}{\delta}\right)\dfrac{T_{max}}{\lambda_{cr}} & \text{if } u \leqslant \lambda_{cr} \\ T = \dfrac{(1-u)}{\delta}\dfrac{T_{max}}{(1-\lambda_{cr})} & \text{if } \lambda_{cr} < u \leqslant 1 \end{cases} \quad (39)$$

where T_{max} is the maximum strength of the cohesive surface, δ is the maximum separation and λ_{cr} is the critical displacement jump such that the interface fails when $u \geqslant \lambda_{cr}\delta$. Fig. 15(a) shows the curve T–u represented in the non-dimensional axes T/T_{max} and u/δ. In principle, T_{max} and δ are given by the mechanical properties of the material. For

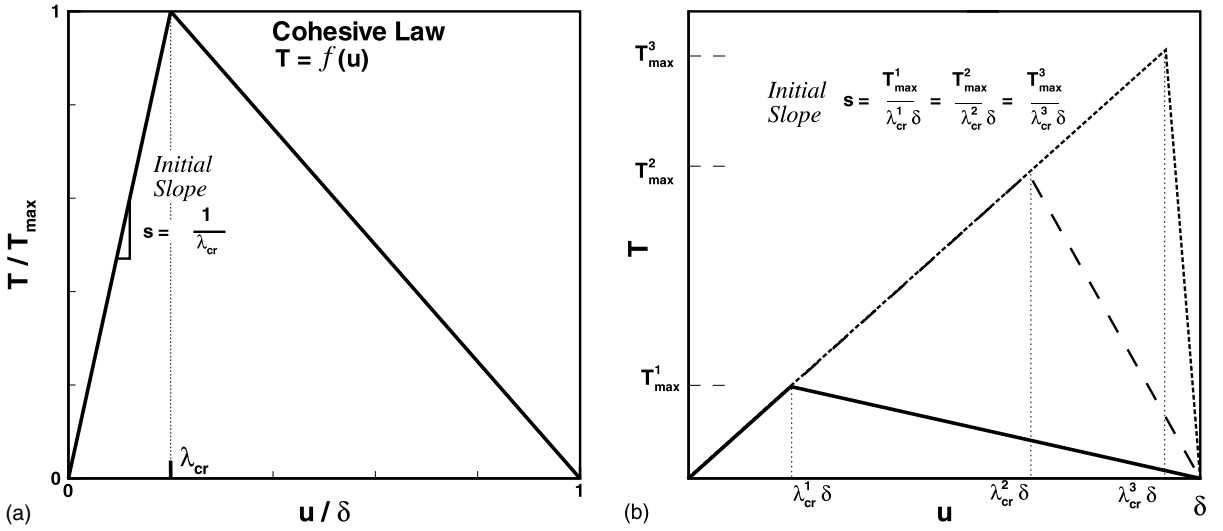

Fig. 15. (a) Traction–separation relation T–u for cohesive law II represented in the non-dimensional axes $T/T_{\max}$ and u/δ. (b) Traction–separation law for three different $T_{\max}$ and same slope; the function is represented on axes T and u.

instance, the critical energy release rate of the interface, which is related to the fracture toughness of the material, is given by

$$G_c = \int_0^{\delta} T(u)\,\mathrm{d}u \tag{40}$$

If $T_{\max}$ and G_c are determined by specially designed experiments, δ can be obtained directly from Eq. (40).

The value of λ_{cr} is selected such that the wave speeds in the material with interfaces are the same as the ones without interfaces during reversible loading. According to the traction–separation relation (T–u) of the cohesive laws II and III, the initial slope is given by

$$\mathbf{s} = \frac{T_{\max}}{\lambda_{\mathrm{cr}}\delta} \tag{41}$$

This slope works as a penalty parameter. In fact as **s** grows, the wave speed in the material asymptotically approaches the speed of the material without interfaces. Hence, this parameter has to be large enough to be effective but not so large as to provoke numerical instabilities. An alternative approach is used by Camacho and Ortiz (1996) and Ortiz and Pandolfi (1999), which in turn corresponds to $\mathbf{s} = \infty$ (ideal case). However, in their approach the discretization is constantly changing as new cohesive elements are added to the mesh. Here we propose a fixed discretization by choosing the slope **s** such that wave speeds are unchanged.

To illustrate the effect of slope **s**, consider a RVE of the material to be analyzed is represented by two finite element meshes of the same dimension and element size. A cohesive surface with interface elements along a straight line in the middle of the RVE is included in one mesh, as it is shown in Fig. 16. The periodic and viscous boundary conditions described in Section 4 are applied at the top of the RVE to simulate normal, shear or mixed stress waves of a given amplitude σ_{W}. The waves travel through the material in the direction perpendicular to the cohesive surface. The amplitude of the stress wave should be chosen such that no irreversible unloading takes place. Since only the slope is being tested, the analyst can select a very high value for $T_{\max}$, such that $\sigma_{\mathrm{W}} < T_{\max}$, and a very high value for δ (or G_{Ic}) such that a wide range of slopes can be considered varying λ_{cr}. Fig. 15(b) shows the traction–separation curve for different values of $T_{\max}$ and only one value of δ. For a fixed slope, δ has to be large enough such that $\lambda_{\mathrm{cr}} \leqslant 1$ when $T_{\max}$ is increased.

The simulations are performed for different conditions and slopes. In order to evaluate the performance of the cohesive law and examine

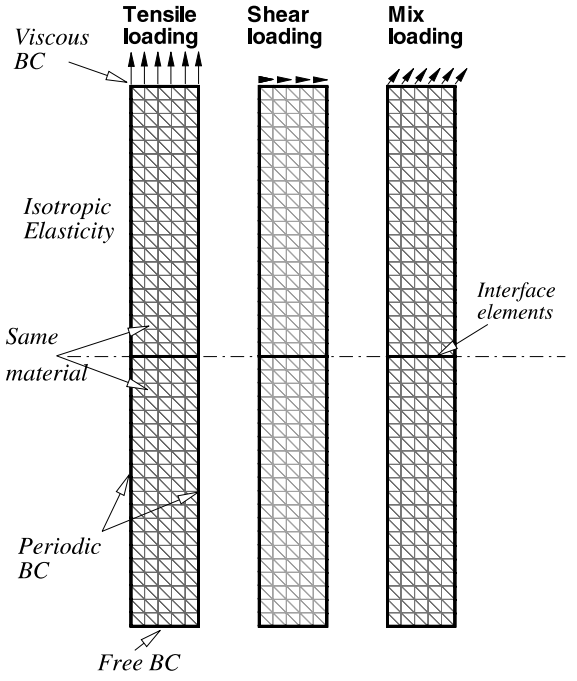

Fig. 16. Finite element mesh used in wave propagation tests. Tension, shear and mixed loading are simulated by viscous boundary conditions. The cohesive surface is located along a straight line oriented perpendicular to the wave path in the middle of the RVE. The mesh without interface elements is not shown.

whether or not there is a numerical instability, the evolution of the tractions at the interface element is evaluated and compared with the stress at the quadrature points of the neighboring elements extrapolated to the cohesive interface, i.e., T_t is compared with σ_{xy} and T_n is compared with σ_{yy}.

Fig. 17(a) shows the evolution of the normal traction T_n evaluated at the cohesive interface elements, compared with the extrapolated σ_{yy} for the cases with and without interface elements when a normal stress wave travels through the material in the direction perpendicular to the cohesive surface. The element size used in these simulations is $h = 1$ μm and the slope $\mathbf{s} = T_{max}/(\lambda_{cr}\delta)$ is given in GPa/μm. The simulations evidently show that for certain values of the initial slopes, the traction at the interfaces, as well as the extrapolated element stress, is well below the traction for the case without interfaces. The higher the slope, the better the traction approaches the ideal solution until instability is achieved for the highest slope. In the case of a slope of 25 000 GPa/μm the instability in T_n is stronger than the extrapolated σ_{yy}, which demonstrates the fact that it is important to test both, T_n and extrapolated σ_{yy}. Fig. 17(b) shows a close up of the evolution of the extrapolated stress at the cohesive interface for all these cases. The convergence is clear in the zoomed region but instabilities can appear at different stages of the wave propagation.

An alternative way, to select λ_{cr} is to compare the initial slope or *stiffness* of the interface with the stiffness of the material. In this way the following constraint can be imposed:

$$\mathbf{s} \gg E/h; \quad \mathbf{s} \geqslant 10E/h \tag{42}$$

where E is the Young modulus of the material and h is the dimension of the volumetric element in the direction perpendicular to the interface. For the case analyzed in Fig. 16, where the young modulus of alumina is about $E = 400$ GPa and the element size $h = 1$ μm, the slope $\mathbf{s}$ must be much higher than 400 GPa/μm, about 10 times E/h, such that the deformation of the material is not affected by the presence of the cohesive interface. In other words, the interfaces become *invisible*.

3.4.2. Cohesive law under compression

Compressive tractions in the interface can also be taken into account directly from the cohesive law. If large displacements and interaction of fragments is expected, a multi-body contact needs to be used, (Espinosa et al., 1998b).

After calculation of (u_n/δ_n) and (u_t/δ_t) if $u_n/\delta_n \leqslant 0$ then the normal component of the traction vector is computed from

$$T_n = \left(\frac{u_n}{\delta_n}\right)\frac{T^0_{max}}{\lambda_{cr}} \tag{43}$$

The tangential component of the traction vector T_t is not affected by this rule except that $\lambda = (u_t/\delta_t)$.

For simulations where there are small displacements, this compressive part of the cohesive law can also be used even after the interface elements have broken. The reason is that the nodes on one grain facet still match the nodes of the other grain. Special care must be taken when there

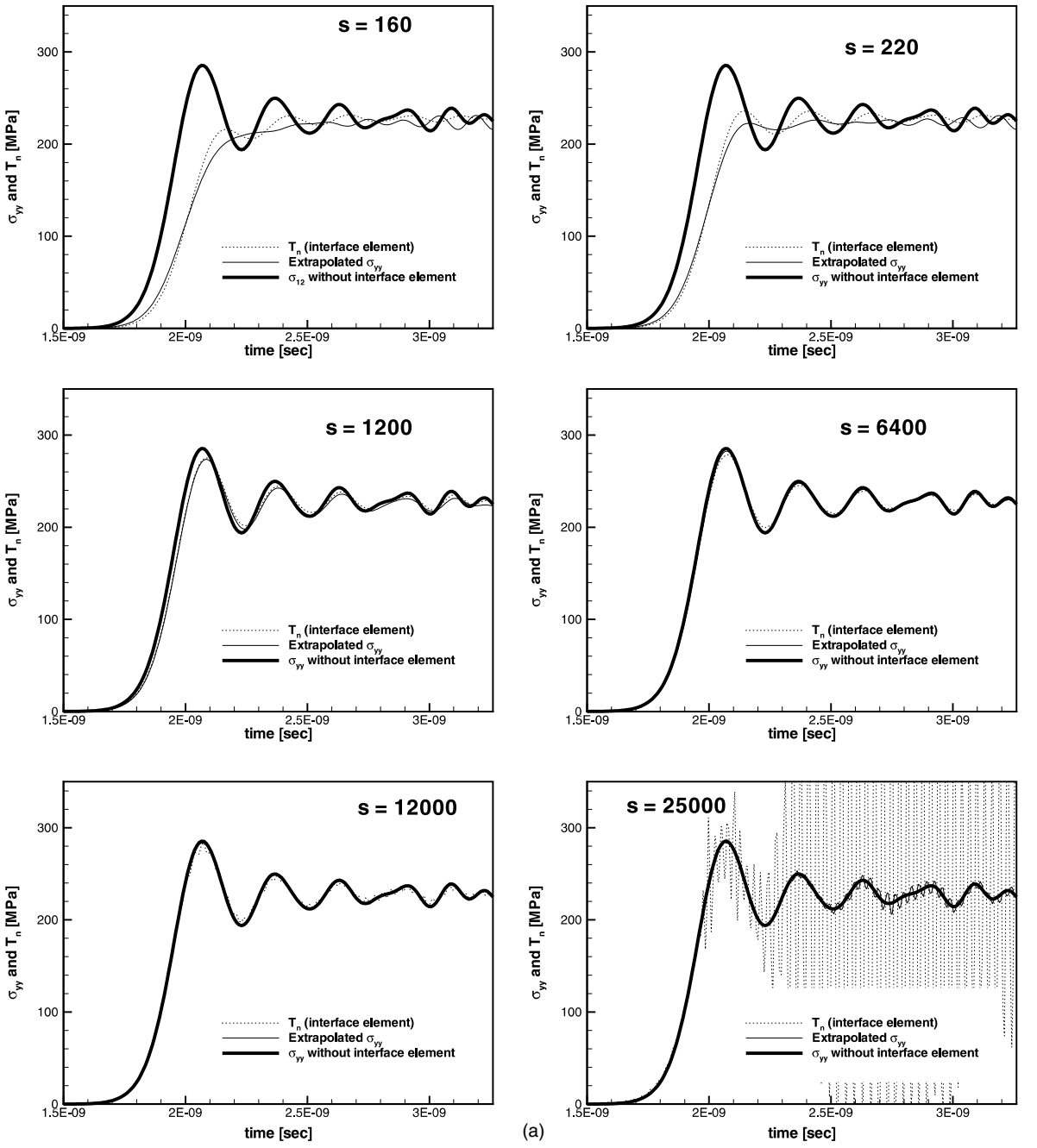

Fig. 17. (a) Extrapolated Cauchy stress and T_n vs time for six different slopes (slopes are given in GPa/μm). (b) Close up showing the extrapolated σ_{yy} for different slopes.

is a transition between small and large displacements, where this law is no longer valid and it must be switched to the multi-body contact algorithm.

3.4.3. Time step calculation

In contrast with the standard explicit schemes, where the time step is solely limited by element

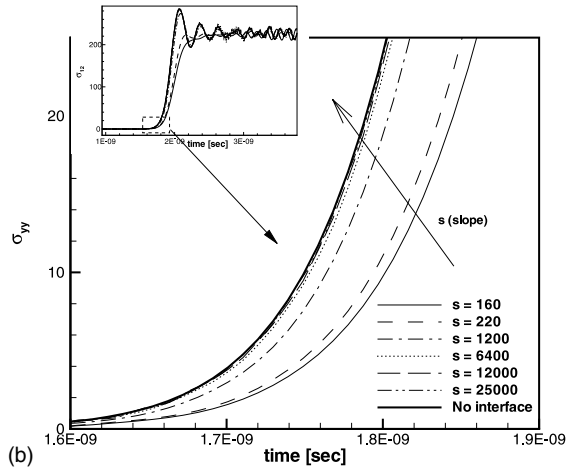

Fig. 17 (*continued*)

stability in order to ensure that waves do not propagate through the mesh faster than the material wave speed, this algorithm considers an additional limitation in the time step as a result of the cohesive law.

As it can be seen in Fig. 4, the cohesive interface law II consists only of two parts $0 \leqslant \lambda < \lambda_{cr}$ and $\lambda_{cr} \leqslant \lambda \leqslant 1$. The time step has to be such that the evolution of λ can follow the cohesive law curve in several time steps. This is accomplished by taking

$$\Delta t_{\text{cohesive}} = \frac{\Delta t_{\text{continuum}} \mathscr{F}}{\max_i \zeta_i} \tag{44}$$

where ζ_i is defined by each interface element i as:

$$\zeta_i = \begin{cases} \dfrac{\Delta\lambda}{\lambda_{cr}} & \text{if } 0 \leqslant \lambda < \lambda_{cr} \\ \dfrac{\Delta\lambda}{1-\lambda_{cr}} & \text{if } \lambda_{cr} \leqslant \lambda < 1 \end{cases} \tag{45}$$

In the above equation $\Delta\lambda = \hat{\lambda}_{n+1} - \lambda_n$ where $\hat{\lambda}_{n+1}$ is the displacement jump predictor for interface i. $\mathscr{F}$ is the inverse of the number of steps required for λ to go from 0 to λ_{cr}.

In this way, the overall time step is taken as

$$\Delta t = \min(\Delta t_{\text{cohesive}}, \Delta t_{\text{continuum}}) \tag{46}$$

where $\Delta t_{\text{continuum}}$ is the stable time step calculated from the maximum six-noded element frequency in the mesh $\omega_{\max}$ (Espinosa et al., 1998b).

One of the limitations of the contact/interface algorithm is that it is very susceptible to instabilities if the time step changes suddenly. As mentioned before, the time step is controlled by the variation in time of the interface element displacement jump, $\dot{\lambda}$, which can change suddenly from one step to another by more than one order of magnitude depending on the contact conditions of the interface element. This may lead to numerical instabilities unless precautions are taken. In order to avoid these instabilities, each element (six-noded and interface elements) is advanced in time with the Δt computed by Eq. (46), while the contact algorithm is advanced in time with $\Delta t_{\text{continuum}}$. Considering that the multi-body contact algorithm is one of the most time consuming parts of the micromechanical model, it can be said that this *subcycling* algorithm not only solves stability problems, but also can provide some speed up in the calculation.

3.4.4. Rate and temperature effects

Rate and temperature effects in the interface description can be easily incorporated in terms of the λ. For law I we have,

$$T_{\max} = T^0_{\max}\left(1 + \zeta \ln\left[\frac{\dot{\lambda}}{\dot{\lambda}_0}\right]\right)\left(1 - \frac{[\Theta - \Theta_0]}{[\Theta_m - \Theta_0]}\right)^{\gamma}$$
$$\text{with} \quad T^0_{\max} = \frac{48 G_c}{27 \delta_n} \tag{47}$$

In the above expression, $T_{\max}$ is the maximum interface traction at the current displacement jump rate $\dot{\lambda}$ and current temperature Θ, $T^0_{\max}$ is the maximum interface traction at reference displacement jump rate $\dot{\lambda}_0$ and reference temperature Θ_0, and Θ_m is a characteristic material temperature. The parameters ζ and γ can be identified through specially designed experiments. Since there are three parameters and only one energy equation, a proper characterization requires a variety of experiments interrogating rate and temperature effects. Likewise, the functional dependence of the interface traction on displacement jumps and temperature needs intensive experimental characterization. The role of rate effects in the failure of alumina was assessed by Zavattieri and Espinosa (2001). Rate effects were also investigated in metals by Lee and Prakash (1999).

4. Initial and boundary conditions in plate impact experiments

The grain level model being presented will be used to model plate impact wave propagation experiments. In this context, initial and boundary conditions need to be defined. In these subsections we address this feature of the simulations.

Due to specimen dimensions in plate impact experiments, such as the material grain size and the number of triangular elements per grain, certain considerations and assumptions can be made in order to avoid computationally expensive calculations. For the dynamic analysis of ceramic microstructure subjected to multi-axial dynamic loading a RVE is considered. Let us consider the example of Fig. 18, in which materials A and B can represent either part of the specimen that remains undamaged and elastic or other materials (i.e., flyer and target plate). Compression and shear waves are either produced at the interface between material A and specimen or transmitted from material A. These waves are in turn transmitted from the specimen to material B. Assuming that materials A and B remain elastic throughout the deformation process, the computational effort can be minimized by replacing materials A and B with viscous boundary conditions based on one-dimensional elastic wave theory. The material A–specimen interface is located at $y = H$, while the specimen–material B interface is located at $y = 0$.

Considering point 1 at material A and point 2 at the interface between material A and specimen, conservation of momentum and continuity of velocities and tractions ($\mathbf{t} \pm (\rho c)v = \text{constant}$), lead to the following equation for tractions t_x and t_y at $y = H$, point 2 in Fig. 18,

$$t_x(x,H,t) = (\rho c_s)_A[v_x(x,H,t) - v_x^1] + t_x^1 \tag{48}$$

$$t_y(x,H,t) = (\rho c_l)_A[v_y(x,H,t) - v_y^1] + t_y^1 \tag{49}$$

For $y = 0$, point 3 in Fig. 18,

$$t_x(x,0,t) = (\rho c_s)_B v_x(x,0,t) \tag{50}$$

$$t_y(x,0,t) = (\rho c_l)_B v_y(x,0,t) \tag{51}$$

where $(\ )_A$ and $(\ )_B$ denote material A and B quantities, c_l and c_s are longitudinal and shear wave speeds, ρ is the specific material density, v_x and v_y are in-plane and normal velocities. The in-plane and normal velocities of material A at point 1 and time zero v_x^1 and v_y^1, as well as the traction t_x^1

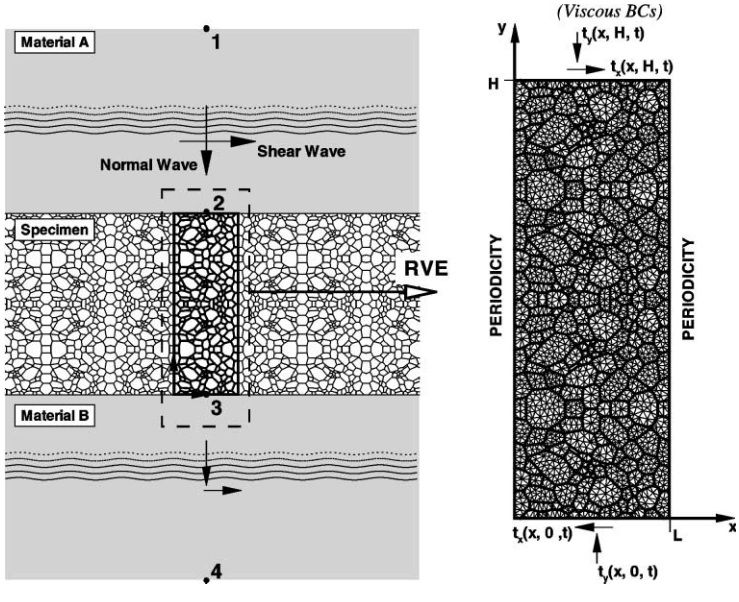

Fig. 18. Schematic of boundary and initial conditions.

and t_y^1 are known values based on one-dimensional wave theory. In addition, the condition of uniform **u**, **v** and **a** at the material A–specimen and specimen–material B interfaces is imposed by averaging the quantities at the top and bottom nodes of the specimen.

For the case where the wave passing through the specimen reflects on a free surface and returns to the specimen, the velocities and forces are summed at the interface between specimen and elastic materials so that they are later used together with Eqs. (48)–(51) to simulate the reflection of the wave.

Assuming that the computational cell is repeated in the x-direction, the following periodic boundary conditions are applied

$$\mathbf{u}(0,y,t) = \mathbf{u}(L,y,t) \quad \mathbf{v}(0,y,t) = \mathbf{v}(L,y,t)$$
$$\mathbf{a}(0,y,t) = \mathbf{a}(L,y,t) \tag{52}$$

where L is the period, and **u**, **v** and **a** are the displacement, velocity and acceleration vector fields. Grains with nodes at $x = 0$ must have the same principal material directions as the grain with nodes at $x = L$ in order to ensure periodicity. Special care at the mesh generation stage must be taken in order to assure the same number of elements and nodal points on both sides of the RVE.

5. Explicit integration scheme

An explicit central-difference integration algorithm is being used to integrate the system of spatially discretized ordinary differential equations in time. The algorithm, accounting for acceleration corrections due to contact, is summarized in Table 1. As in any initial boundary value problem, initial displacements and velocities, $\mathbf{u}^0$ and $\mathbf{v}^0$, are required. Initial accelerations $\mathbf{a}_0$ are calculated from initial applied forces $\mathbf{f}_0^{\text{ext}}$ and initial internal forces $\mathbf{f}_0^{\text{int}}$.

At each time step n, the nodal accelerations must first be corrected for any time-dependent changes in the traction boundary conditions. Then, a displacement predictor at time $n+1$ is computed using the corrected acceleration and the displacements and velocities at time step n. Modified accelerations at time n, $\Delta\mathbf{a}_n$, are computed based on the corrected acceleration and changes in accelerations resulting from surface contact determined from the displacement predictor at $n+1$. Updated displacements at $n+1$ are used in the update of stresses and the computation of internal forces. In contrast with the original algorithm presented by the authors (Espinosa et al., 1998b), the correction of the accelerations is multiplied by a different time step ($\Delta t_{\text{contact}}$) described in Section 3. Lastly, accelerations and velocities at time $n+1$ are obtained completing the time integration scheme. Corrected accelerations at step (3) need to be computed. These correction terms arise from changes in the applied boundary traction due to changes in the applied external forces, (Espinosa et al., 1992). If such corrections are not incorporated in the numerical implementation, spurious oscillations are introduced with magnitudes proportional to the traction change.

Correction of the accelerations due to changes in the traction in the interface element has been also included in the algorithm. This correction consists in adding an extra term in the acceleration of the nodes that belong to interface elements. $\Delta a = (\widehat{T}_{n+1} - T_{\text{n}})/M$ where $\widehat{T}_{n+1}$ is the traction at the interface element calculated using the displacement predictor.

6. Modeling of stochastic effects

The interfaces between different material phases are important in determining many bulk properties. One of the simplest interface types is the boundary between two crystals of the same material. If two crystals of exactly the same orientation are brought together, they fit perfectly. However, if the crystals are slightly tilted, there is a disregistry at the interface, which is equivalent to insertion of a row of dislocations. The number of dislocations per unit length and the energy of the boundary increase as the angle of tilt increases. If instead of being tilted, the two grains are rotated or twisted, the result is a grid of screw locations that are more complex to represent diagrammatically but are basically similar to the tilt boundary. A combined tilt and rotation corresponds to a

Table 1
Explicit integration algorithm

1. Initial conditions:
$t = 0$, $t_{\text{contact}} = 0$, $n = 0$, $\mathbf{u}_0 = \bar{\mathbf{u}}_0$, $\mathbf{v}_0 = \bar{\mathbf{v}}_0$, $\mathbf{t}_0 = \bar{\mathbf{t}}_0$
$\mathbf{a}_0 = (\mathbf{f}_0^{\text{ext}} - \mathbf{f}_0^{\text{int}})/\mathbf{M}$ where

$$\begin{cases} \mathbf{f}_0^{\text{int}} = \int_{B_0} \mathbf{B}^T \tau_0 \, \mathrm{d}B_0 & \text{all elements} \\ \mathbf{f}_0^{\text{ext}} = -\text{area}(\rho c)_f \mathbf{v}_0 & \text{viscous boundary} \\ \mathbf{f}_0^{\text{ext}} = \int_{S'} N_s^T T \, \mathrm{d}S' & \text{cohesive interface} \end{cases}$$

2. Compute $\Delta t = \min(\Delta t_{\text{cohesive}}, \Delta t_{\text{continuum}})$

$$\begin{cases} \Delta t_{\text{continuum}} < 2/\omega_{\max} & \text{for triangular elements} \\ \Delta t_{\text{cohesive}} & \text{for interface elements} \end{cases}$$

and $t = t + \Delta t$
3. Correct accelerations due to changes in boundary forces:
$\mathbf{a}_n = \mathbf{a}_n + \frac{\mathbf{t}_{n+1} - \mathbf{t}_n}{\mathbf{M}}$, $\mathbf{f}^{\text{ext}} = \int_{S'} N_S^T \mathbf{t} \, \mathrm{d}S'$
where $\mathbf{t}$ is obtained from viscous boundary conditions

4. Compute displacement predictor:

$$\begin{cases} \hat{\mathbf{u}}_{n+1} = \mathbf{u}_{\text{n}} + \triangle t \mathbf{v}_{\text{n}} + \frac{1}{2} \triangle t^2 \mathbf{a}_n & \text{all elements} \\ \hat{\mathbf{u}}_{n+1} = \mathbf{u}_{\text{n}} + \triangle t \mathbf{v}_{\text{n}} + \frac{1}{2} \triangle t^2 \left(\mathbf{a}_n - \dfrac{\text{area}(\rho c)_f (\mathbf{v}_{\text{n}} - \mathbf{v}_{n-1})}{\mathbf{M}} \right) & \text{viscous boundary} \end{cases}$$

5. If $t \geqslant t_{\text{contact}} + \Delta t_{\text{continuum}} \Rightarrow$ compute $\triangle \mathbf{a}_n$ (correction of the accelerations due to contact)
The forces on the slave nodes are computed with the time step $\Delta t_{\text{contact}} = t - t_{\text{contact}}$.
$t_{\text{contact}} = t$
Otherwise $\Delta \mathbf{a}_n = 0$
The contact is not computed for interface elements whose compressive part is governed by Eq. (43)

6. Compute $\hat{\mathbf{f}}_{n+1}^{\text{ext}} = \int_{S'} N_s^T \widehat{T}_{n+1} \, \mathrm{d}S'$ for interface elements, where $\widehat{T}_{n+1} = f(\hat{\mathbf{u}}_{n+1})$ from cohesive law.
Update the acceleration for interface elements:

$$\Delta a = \Delta a + (\hat{\mathbf{f}}_{n+1}^{\text{ext}} - \mathbf{f}_{\text{n}}^{\text{ext}})/\mathbf{M}$$

7. Update displacements:

$$\begin{cases} \mathbf{u}_{n+1} = \mathbf{u}_{\text{n}} + \triangle t \mathbf{v}_{\text{n}} + \frac{1}{2} \triangle t^2 \mathbf{a}_n + \frac{1}{2} \triangle t_{\text{contact}}^2 \triangle \mathbf{a}_n & \text{all elements} \\ \mathbf{u}_{n+1} = \mathbf{u}_{\text{n}} + \triangle t \mathbf{v}_{\text{n}} + \frac{1}{2} \triangle t^2 \left(\mathbf{a}_n - \dfrac{\text{area}(\rho c)_f (\mathbf{v}_{\text{n}} - \mathbf{v}_{n-1})}{\mathbf{M}} \right) + \frac{1}{2} \triangle t_{\text{contact}}^2 \triangle \mathbf{a}_n & \text{viscous boundary} \end{cases}$$

8. Impose periodic boundary conditions on the displacements $\mathbf{u}_{n+1}$
9. Update $\overline{\mathbf{S}} = \overline{\mathbf{S}}(\mathbf{u}_{n+1})$ and compute internal force vector:

$$\begin{cases} \mathbf{f}_{n+1}^{\text{int}} = \int_{B_0} \mathbf{B}^T \tau_{n+1} \, \mathrm{d}B_0 & \text{all elements} \\ \mathbf{f}_{n+1}^{\text{ext}} = -\text{area}(\rho c)_f \mathbf{v}_{\text{n}} & \text{viscous boundary} \\ \mathbf{f}_{n+1}^{\text{ext}} = \int_{S'} N_s^T T \, \mathrm{d}S' & \text{cohesive interface.} \end{cases}$$

10. Solve for accelerations:
$\mathbf{a}_{n+1} = (\mathbf{f}_{n+1}^{\text{ext}} - \mathbf{f}_{n+1}^{\text{int}})/\mathbf{M}$

11. Update velocity vector:

$$\begin{cases} \mathbf{v}_{n+1} = \mathbf{v}_{\text{n}} + \frac{\triangle t}{2} (\mathbf{a}_n + \mathbf{a}_{n+1}) + \frac{1}{2} \triangle t_{\text{contact}} \triangle \mathbf{a}_n & \text{all elements} \\ \mathbf{v}_{n+1} = \mathbf{v}_{\text{n}} + \frac{\triangle t}{2} \left(\mathbf{a}_n + \mathbf{a}_{n+1} - \dfrac{\text{area}(\rho c)_f (\mathbf{v}_{\text{n}} - \mathbf{v}_{n-1})}{\mathbf{M}} \right) + \frac{1}{2} \triangle t_{\text{contact}} \triangle \mathbf{a}_n & \text{viscous boundary} \end{cases}$$

12. Impose periodic boundary conditions on the velocities $\mathbf{v}_{n+1}$

13. $n = n + 1$, if $n < n_{\max}$ go to step (2), else stop

complex combination of edge and screw dislocations. There is a well-known model that characterizes the structural order at grain boundaries through a parameter that measures the reciprocal density of co-incident lattice sites (Σ), the so-called co-incident-site lattice model (Bollmann, 1970).

Low values of Σ correspond to a high density of co-incident lattice sites. Atomistic computations (Tasker and Duffy, 1983; Wolf, 1984), reveal that special low energy interfaces are found for $\Sigma < 29$. It was observed that there is a tendency for boundaries with $\Sigma < 29$ to be resistant to cracking and those with $\Sigma > 29$ to be susceptible to cracking. Boundaries with $\Sigma > 29$ are referred to as random boundaries. Fig. 19(a) shows a high resolution transmission electron microscope (HRTEM) picture of a high-angle alumina–alumina interface (Espinosa, 1992).

Several investigators have studied the interfacial properties of Al_2O_3 containing SiC nanoparticles along grain boundaries by means of transmission electron microscopy (TEM) (Jiao et al., 1997; Luo and Stevens, 1997; Sternitzke, 1997). They found that the magnitude of the interfacial fracture energy between SiC and alumina is over twice the alumina grain boundary fracture energy. Therefore grain boundaries are strengthened by the addition of SiC nanoparticles. The location of SiC nanoparticles along grain boundaries is not uniform but rather quite inhomogeneous.

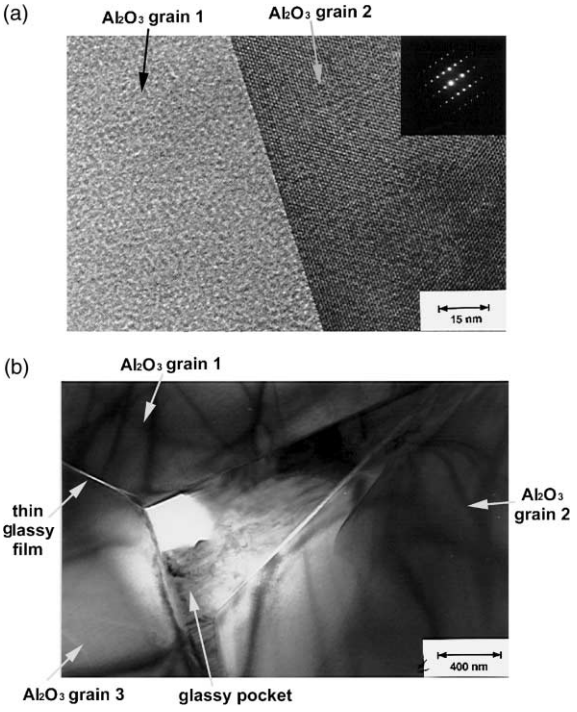

Fig. 19. (a) HRTEM image of a typical high angle grain boundary. (b) TEM bright field image of a glass pocket in alumina.

Another factor affecting grain boundary fracture energy is the the presence of glassy phase and glass pockets. Either from impurities present in the powder, sintering aids, and/or contaminants transported through the vapor phase from the hot furnace or container walls to the material being fired, a second phase is sometimes formed at the grain boundaries of ceramics. This second phase has an amorphous structure. High resolution electron microscopy micrographs were obtained by Espinosa (1992), at the interface of alumina and a glass pocket (see Fig. 19(b)).

The random distribution of glass pockets, glassy phases, SiC nanoparticles, defects and other impurities leads to the consideration of a statistical variation in the interfacial strength dependent on the grain misorientation. Data on grain boundary toughness as a function of co-incident lattice sites are very limited and incomplete in the literature. For this reason, the stochasticity of the microfracture process with distributions which are independent of the principal material directions, is considered in the analysis. With advances in atomistic models, the grain boundary fracture strength can be estimated as a function of grain boundary tilt and twist from first principles.

6.1. Weibull distributions

If a large number of identical samples were to be tested and the strength distribution of a brittle and a ductile solid plotted, they would look quite different. The strength distribution curve for ductile solids is very narrow and close to a *Gaussian* or *normal distribution*, while that for brittle solids is very broad with a large tail on the hit-strength side that can be explained by a statistical distribution called the *Weibull distribution*, named after the

Swedish engineer who first proposed it (Weibull and Sweden, 1951).

In this analysis, the interfacial strength parameters will be described by a *Weibull* distribution. Since only two interface parameters can be varied, two distributions will be considered: varying K_{IC} and keeping T_{max} constant, viceversa and varying both at the same time.

The Weibull distribution for K_{IC} and T_{max} are:

$$f(K_{IC}) = \frac{m(K_{IC})^{m-1}}{K_{IC}^{0\ m}} \exp\left[-\left(\frac{K_{IC}}{K_{IC}^0}\right)^m\right], \quad K_{IC} > 0 \tag{53}$$

$$f(T_{max}) = \frac{m(T_{max})^{m-1}}{T_{max}^{0\ m}} \exp\left[-\left(\frac{T_{max}}{T_{max}^0}\right)^m\right], \quad T_{max} > 0 \tag{54}$$

where K_{IC}^0 and T_{max}^0 are material constants and m is the *Weibull modulus*, which is a measure of the variability of the strength of the material. Generally, $m = 3$–10 for the case of brittle ceramic samples. Fig. 20 shows several Weibull distributions for K_{IC} using different values for K_{IC}^0 and m.

The distribution is randomly generated such that a grain facet will have the same interface element parameters. In this way there will be only N_f different interface elements (N_f = number of facets in the microstructure). Fig. 21 shows an example where each grain facet contains different values of T_{max} and K_{IC}. Fig. 21(a) shows the variation of T_{max} with different intensities of gray. The histogram for T_{max} and K_{IC} is shown in Fig. 21(b).

6.2. Glassy phase, glass pockets and initial defects

This micromechanical model lends itself to the consideration of material defects. For example depending on the purity and porosity of the ceramic, intergranular glassy phase, glass pockets, porosity, and other initial flaws can be explicitly included in the RVE.

Grain boundary shearing due to the presence of an intergranular nanometer glass layers can be easily incorporated in the model by means of the interface cohesive law III presented in Section 3.3. Only a limited number of grain facets is modeled by interface elements governed by this law. Interfaces between grains without glassy phase are simulated with interface elements using law II (Section 3.2).

Glass pockets at a triple junction, as shown in Fig. 19(b), can also be included in the model. For this, special care must be taken at the mesh generation stage to include the shape of the glass pockets. The material properties of the glass are assigned to the elements contained in the glass pockets. Interface elements between glass pockets

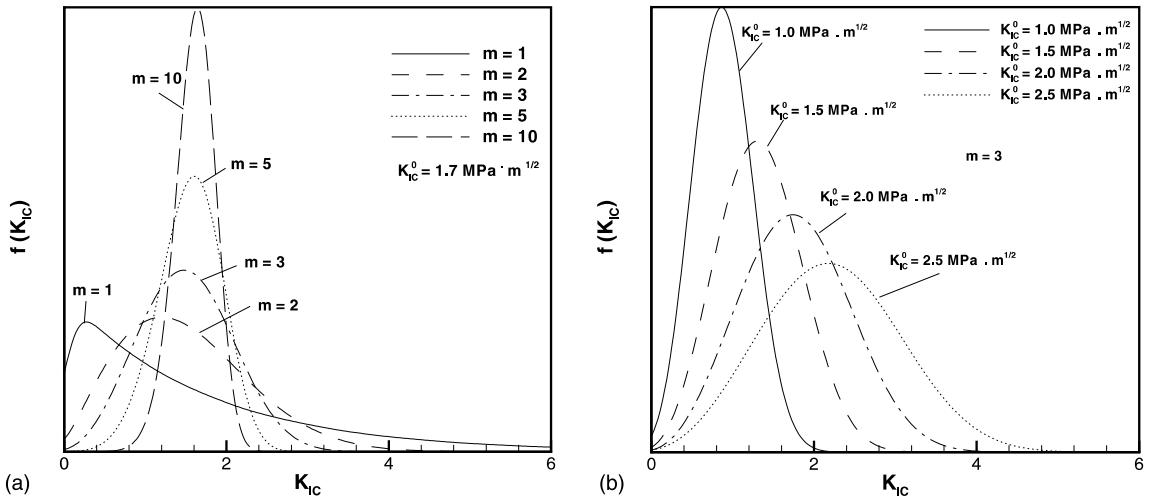

Fig. 20. Plots of Weibull distributions for (a) $m = 1$, 2, 3, 5 and 10; (b) $K_{IC} = 1$, 1.5, 2 and 2.5 MPa $\sqrt{m}$.

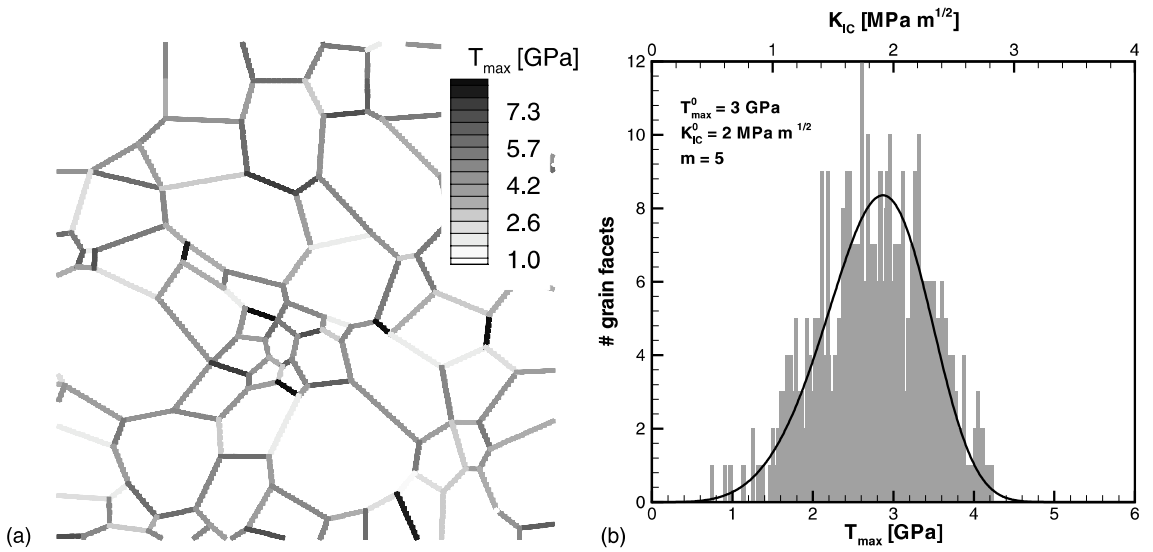

Fig. 21. Example of a Weibull distribution for interface parameters in a typical microstructure. (a) The different intensities of gray indicate the value of $T_{\max}$, dark lines represent grain facet with higher values of $T_{\max}$. (b) Histogram for $T_{\max}$ and K_{IC}.

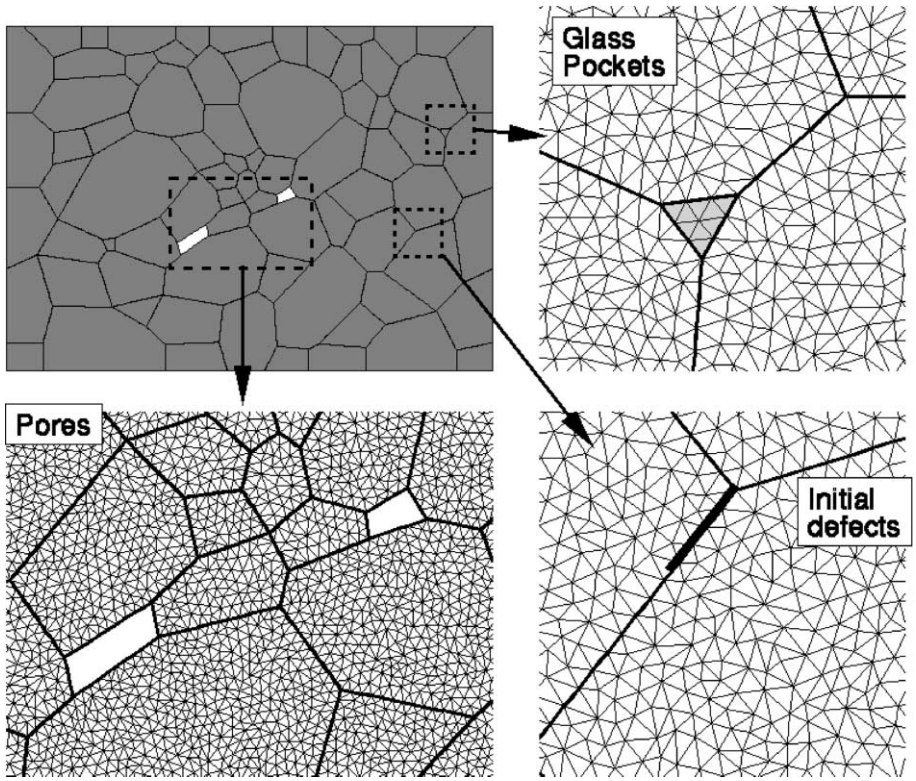

Fig. 22. Schematics of a ceramic microstructure with initial defects, pores and glass pockets.

and grains are governed by law III as for the case of nanometer film glassy layer. Fig. 22 shows an example where the microstructure contains glass pockets. A similar procedure can be done for the case of pores, where the pores are represented by regions without finite elements (see Fig. 22).

During the process of sintering, microcracks can nucleate at triple grain junctions during cooling. This results in a set of initial microcracks. An initial distribution of flaws can be included in the model deleting some of the interface elements next to a triple point. The number of interface elements determines the length of the initial defect (usually $\approx$10% of the face length). Fig. 22 shows, with a thicker line, an initial defect at a triple point. As it will be shown in part II of this work, a microstructure with an initial distribution of flaws, which can be a more realistic case to analyze, is more susceptible to microfracture than an "*ideal*" microstructure without defects. It should be noted that an accurate determination of microcracks and residual stresses, resulting from material sintering, can be obtained by modeling the cooling process of the same RVE.

7. Modeling residual thermal stresses and thermal induced microcracking

Throughout this study, the ceramic microstructure has been idealized as an ensemble of randomly oriented, elastically and thermally anisotropic grains with brittle intergranular interfaces. In the process of cooling, the solid is brought from its fabrication temperature down to some final conditions, typically room temperature. The stresses in the sample are assumed to be relaxed at the fabrication temperature due to creep. During this cooling process, the body develops microstructural residual stresses due to thermal and elastic anisotropy of grains. The cooling is assumed to be slow enough so that the temperature remains nearly uniform over the body at all times. This leads to an incremental quasi-static analysis where the temperature is decreased by a prescribed amount until room temperature is reached. Under the assumption of the analysis, the response of each grain is characterized by its elastic anisotropic material stiffness tensor $\mathscr{C}_{ijkl}$ and its thermal expansion co-efficients α_{ij}. The components of these tensors on some global Cartesian reference frame (x,y,z) depend on the orientation of the grain, as described in Section 2.2.1. The stress–strain relation including thermal strains can may be expressed as:

$$S_{ij} = \mathscr{C}_{ijkl}(H_{kl} - H^0_{kl}) \tag{55}$$

where $\mathscr{C}$ is the elastic anisotropic material stiffness tensor in the global co-ordinates (x,y,z) and H^0 is the strain tensor resulting from thermal contraction, such that

$$H^0_{ij} = \alpha_{ij}\Delta T$$

ΔT denotes the cooling range and α_{ij} the tensor of linear thermal expansion co-efficients defined in the global co-ordinates. In the case of anisotropic crystals, the elastic constitutive matrix $\widehat{\mathscr{C}}_{IJKL}$ and the thermal expansion co-efficients $\hat{\alpha}_{IJ}$ are defined in the local co-ordinate system of the grain by their principal material directions $(1,2,3)$, such that

$$\begin{aligned} \mathscr{C}_{ijkl} &= \mathbf{T}^c_{iI}\mathbf{T}^c_{jJ}\mathbf{T}^c_{kK}\mathbf{T}^c_{lL}\widehat{\mathscr{C}}_{IJKL}, \\ \alpha_{ij} &= \mathbf{T}^c_{iI}\mathbf{T}^c_{jJ}\hat{\alpha}_{IJ} \end{aligned} \tag{56}$$

where $\mathbf{T}^c$ is the transformation matrix. As discussed in Section 2.2.1, each grain is assumed to be elastic orthotropic and the orientation of the principal material directions differs from grain to grain. As previously mentioned, the process of cooling is considered as an incremental quasi-static analysis where the temperature is decreased by steps. In each step the static analysis solves nonlinear equation $(\mathbf{K} + \mathbf{K}_{\mathrm{I}})\mathbf{d} = \mathbf{R}_{\mathrm{T}}$ where $\mathbf{K}$ is the element stiffness matrix representing the anisotropic elastic behavior of the single crystal grains, $\mathbf{K}_{\mathrm{I}}$ is the interface element stiffness matrix, $\mathbf{d}$ is the nodal displacement vector and $\mathbf{R}_{\mathrm{T}}$ is the thermal load vector. More details on this quasi-static model and its implementation can be found in Zavattieri (2000).

8. Microcrack evolution and stereology

An important feature of the proposed model is its capability of producing microcrack patterns

and evolution of crack densities. The issue is how to describe these results with a single weighted parameter. In this section crack surface per unit volume is defined and its function illustrated. Consider a RVE under the dynamic conditions described in Section 4. Fig. 23 shows the evolution of crack pattern along the whole microstructure for a typical calculation. As the wave front advances, crack nucleation and growth occurs up to the moment when the wave reaches the bottom face. As described earlier, once the effective displacement jump exceeds a value of 1, the interface elements are assumed to have failed and a microcrack is said to have initiated at that grain boundary. As all grain boundaries are embedded with interface elements, the lines shown in Fig. 23 indicate the boundary of the grains that have failed during loading. Subsequent failure of neighboring interface elements leads to microcrack propagation and coalescence. Although crack patterns provide understanding of the process of microfracture inside the ceramic, the use of stereology provides more insight into the different damage mechanisms.

Quantitative stereology attempts to characterize numerically geometrical aspects of the microstructure. Underwood (1970), presented a technique to extrapolate information from 2D crack lines to 3D complex crack surfaces. The technique provides and estimate of microcrack surface area per unit volume, S_v. By equating the total crack surface area per unit volume, S_v, to twice the average value of the number of intersections of a set of test lines of unit length P_L, an estimate of S_v can be obtained. P_L is the‘ number of intersections/(number of lines $\times$ length of each line/magnifi cation). For anisotropic microstructures, the number of intersections of a set of test lines, with the boundaries of microcracks, depends on the angular orientation of the test lines in the plane. Thus, in order to obtain a representative average value of the intersection count, it is important to perform the measurements on different angular orientations in the cross-section in question. The dependence of the number of intersections per unit length with the angle of the test lines can be used to characterize the degree of microcracking anisotropy.

After obtaining $S_v(\mathbf{t})$, $\dot{S}_v(t)$ can be calculated by numerical differentiation. Fig. 24 (left) shows the evolution of $S_v(\mathbf{t})$ and $\dot{S}_v(t)$ from the time the specimen is loaded, up to 500 ns. Moreover, the angular crack density distribution $S_v(\theta, \mathbf{t})$ can be calculated, and the rosette shown in Fig. 24 (right) can be constructed. Each point x, y in this rosette is defined as

$$x = S_v(\theta \pm \Delta\theta)\cos(\theta) \tag{57}$$

$$y = S_v(\theta \pm \Delta\theta)\sin(\theta) \tag{58}$$

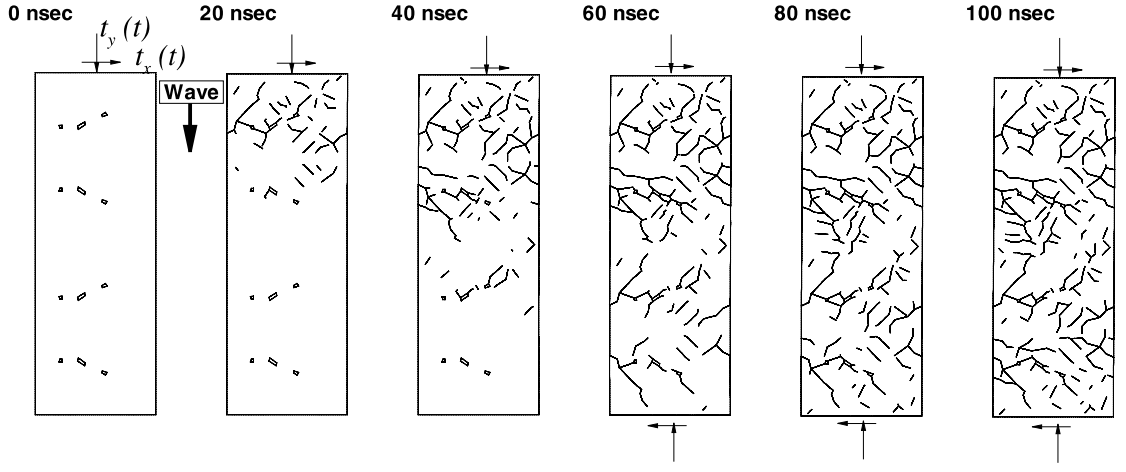

Fig. 23. Crack pattern evolution in a microstructure subjected to multi-axial loading.

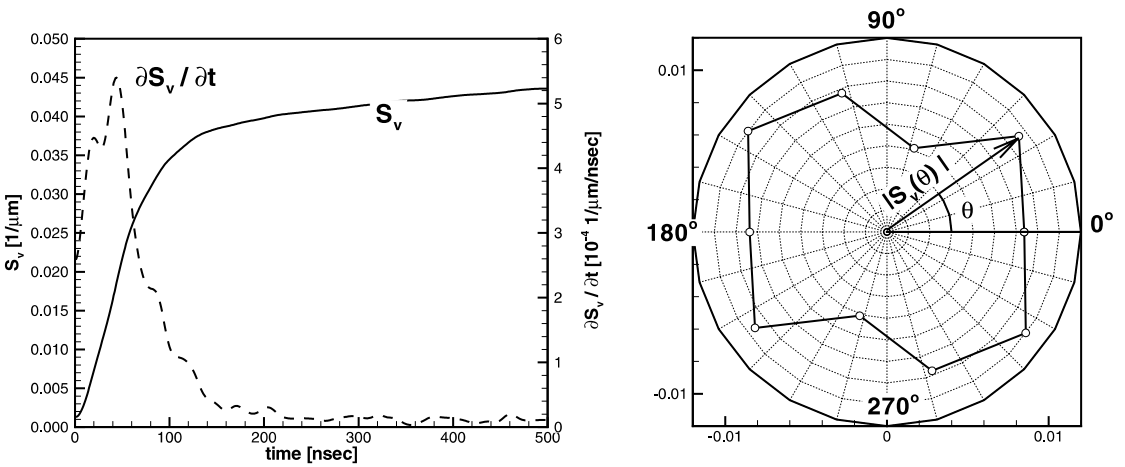

Fig. 24. Plots of $S_v(t)$, $\dot{S}_v(t)$ (left) and $S_v(\theta, t_f)$ (rosette, right) for a microstructure subjected to multi-axial loading.

In other words, the distance from each point to the origin is the crack density for all the cracks with an angular orientation, θ, such that $\theta - \Delta\theta \leqslant \theta < \theta + \Delta\theta$. The degree of discretization is defined as $\Delta\theta = 2\pi/N$, where N is the number of intervals. For example, Fig. 24 (right) is the rosette constructed with a discretization $N = 10$. The reason why a very low discretization factor has been chosen is the small number of potential angles where the crack can occur in the simulated microstructure. Even though these figures show the variation of θ from 0 to 2π, the angle is varied from 0 to π, and the density $S_v(\theta + \pi)$ is assumed equal to the density $S_v(\theta)$. The relationship between $S_v(t)$ and $S_v(\theta, t)$ is $S_v(t) = \int_0^{\pi} S_v(\theta, t)\mathrm{d}\theta$.

9. Concluding remarks

A model was presented to analyze material microstructures subjected to quasi-static and dynamic loading. An RVE composed of a set of grains was introduced with special consideration to the size distribution, morphology, phases and presence and location of initial defects. Stochastic effects were considered in relation to grain boundary strength and toughness. An important feature of the model was highlighted, i.e., its capability to capture the evolution of stress induced microcracking from the material fabrication stage. This feature becomes particularly relevant in the identification of material strength as well as spatial distribution of initial defects.

Intergranular cracking was modeled by means of interface cohesive laws influenced by the physics of breaking of atomic bonds or grain boundary sliding by atomic diffusion. Several cohesive laws were presented and their advantages in numerical simulations discussed. In particular cohesive laws to simulate grain boundary cracking and sliding or shearing were mathematically formulated. The main advantage of the proposed method, in relation to crack initiation, propagation and coalescence as an outcome of the simulations, was also examined.

The equations governing the initial boundary value problem, as well as their numerical implementation, were presented with special emphasis on selection of cohesive law parameters and time step. The importance of avoiding spurious effects, such as the addition of artificial flexibility in the computational cell, was addressed. Simulations reported in part II of this work illustrate this important aspect of the model.

The reader should realize that the grain level model lends itself very well for the examination of novel heterogeneous materials. Percentage and distribution of phases, grain boundary strength

and its variability, microstructure morphology at the micro- and mesoscales can all be accounted for in the proposed framework. A microscale example would be the analysis of a material with variable chemical composition, grain size and/or grain morphology within the computational cell. A mesoscale example would involve the analysis of a multi-layered material in which each layer could have a thickness of a few millimeters. Likewise, the discussed model could be used in relation to the investigation of RVEs of materials or the extension of a single crack in which crack tip material microstructural details are modeled.

A technique for quantifying microcrack density, that can be used in the formulation of continuum micromechanical models, was also discussed. The density was assessed spatially and temporally to account for damage anisotropy and evolution. Although this feature has not been fully exploited, with the continuous development of less expensive and more powerful massively parallel computers, the model is expected to be particularly relevant to those interested in developing new heterogeneous materials and their constitutive modeling. In fact, effects of stochasticity and other material design variables, difficult and expensive to obtain experimentally, will be easily assessed numerically by Monte Carlo grain level simulations. In particular, extension to three-dimensional simulations of RVEs will become feasible. It should be noted that such analyses are needed for a proper quantification of inelasticity and damage field variables.

Acknowledgements

The authors acknowledge ARO and DoD HPCMP for providing supercomputer time on the 128 processors Origin 2000 at the Naval Research Laboratory-DC (NRL-DC). This research was supported by the National Science Foundation through Awards no. CMS 9523113 and CMS-9624364 (NSF-CAREER), the Office of Naval Research YIP through Award no. N00014-97-1-0550, the Army Research Office through ARO-MURI Award no. DAAH04-96-1-0331 and the Air Force Office of Scientific Research through Award no. F49620-98-1-0039.

References

Abraham, F., Brodbeck, D., Rafey, R., Rudge, W., 1994. Instability dynamics of fracture—a computer-simulation investigation. Phys. Rev. Lett. 73 (2), 272–275.

Abraham, F., Brodbeck, D., Rudge, W., Broughton, J., Schneider, D., Land, B., Lifka, D., Gerner, J., Rosenkrantz, M., Skovira, J., Gao, H., 1998. Ab initio dynamics of rapid fracture. Model. Simulat. Mater. Sci. Eng. 6, 639–670.

Addessio, F., Johnson, J., 1999. A constitutive model for the dynamic response of brittle materials. LA-UR-89-2651, Los Alamos National Laboratory, Los Alamos, NM, USA.

Bazant, Z., Oh, B., 1985. Microplane model for progressive fracture of concrete and rock. J. Eng. Mech., ASCE 111 (4), 559.

Belytschko, T., Tabbara, M., 1996. Dynamic fracture using element-free galerkin methods. Int. J. Numer. Meth. Eng. 39, 923–938.

Belytschko, T., Krongauz, Y., Organ, D., Fleming, M., Krysl, P., 1996. Meshless methods—an overview and recent developments. Comput. Meth. Appl. Mech. Eng. 139, 3–47.

Belytschko, T., Organ, D., Gerlach, C., 2000. Element-free galerkin methods for dynamic fracture in concrete. Comput. Meth. Appl. Mech. Eng. 187, 385–399.

Belytschko, T., Moes, N., Usui, S., Parimi, C., 2001. Arbitrary discontinuities in finite elements. Int. J. Num. Meth. Eng. 50, 993–1013.

Bolander, J., Saito, S., 1998. Fracture analyses using spring networks with random geometry. Eng. Fract. Mech. 61, 569–591.

Bollmann, W., 1970. Crystal Defects and Crystalline Interfaces. Springer-Verlag, Berlin.

Camacho, G., Ortiz, M., 1996. Computational modeling of impact damage in brittle materials. Int. J. Solid Struct. 33, 2899–2938.

Curran, D., Seaman, L., Cooper, T., Shockey, D., 1990. Micromechanical model for comminution and granular flow of brittle material under high strain rate application to penetration of ceramic targets. Int. J. Impact Eng. 13, 53–83.

Dwivedi, S., Espinosa, H., 2003. Modeling dynamic crack propagation in fiber reinforced composites including frictional effects. Mech. Mater., in press. PII: S0167-6636(02)00266-1.

Emore, G., 1996. Computational modeling of geometric and material nonlinearities with applications to impact dynamics. Master's thesis, Purdue University.

Espinosa, H., 1992. Micromechanics of the Dynamic Response of Ceramics and Ceramic Composites. Ph.D. Thesis, Brown University, Providence, RI.

Espinosa, H., 1995. On the dynamic shear resistance of ceramic composites and its dependence on applied multiaxial deformation. Int. J. Solid Struct. 32, 3105.

Espinosa, H., Raiser, G., Clifton, R., Ortiz, M., 1992. Performance of the star-shape flyer in the study of brittle materials: Three-dimensional computer simulations and experimental observations. J. Appl. Phys. 72, 3451–3457.

Espinosa, H., Zavattieri, P., Dwivedi, S., 1998a. A finite deformation continuum/discrete model for the description of fragmentation and damage in brittle materials. J. Mech. Phys. Solid 46 (10), 1909–1942.

Espinosa, H., Zavattieri, P., Emore, G., 1998b. Adaptive FEM computation of geometric and material nonlinearities with application to brittle failure. Mech. Mater. 29, 275–305.

Gao, H., 1996. A theory of local limiting speeds in dynamic fracture. J. Mech. Phys. Solid 44, 1453–1474.

Geubelle, P., Baylor, J., 1998. Impact-induced delamination of composites: a 2d simulation. Compos. Part B: Eng. 29 (5), 589–602.

Ghosh, S., Nowak, Z., Lee, K., 1997. Tessellation-based computational methods for the characterization and analysis of heterogeneous microstructures. Compos. Sci. Technol. 57, 1187–1210.

Ghosh, S., Yunshan, L., 1995. Voronoi cell finite element model based on micropolar theory of thermoelasticity for heterogeneous materials. Int. J. Numer. Meth. Eng. 38, 1361–1368.

Grah, M., Alzebdeh, K., Sheng, P., Vaudin, M., Bowman, K., Ostoja-Starzewki, M., 1996. Brittle intergranular failure in 2d microstructures: experiments and computer simulations. Acta Mater. 44 (10), 4003–4018.

Gumbsch, P., Zhou, B., Holian, S.J., 1997. Molecular dynamics of dynamic crack stability. Phys. Rev. B—Condens. Matter 55 (6), 3445–3455.

Helms, K., Allen, D., Hurtado, L., 1999. A model for predicting grain boundary cracking in polycrystalline viscoplastic materials including scale effects. Int. J. Fract. 95, 175–194.

Jiao, S., Jenkins, M., Davidge, R., 1997. Interfacial fracture energy–mechanical behavior relationship in Al_sO_3/SiC and Al_sO_3/TiN nanocomposites. Acta Mater. 45 (1), 149–156.

Johnson, G., Holmquist, T., 1992. A computational constitutive model for brittle materials subjected to large strains, high strain rates and high pressures. In: Meyers, M.A., Murr, L.E., Staudhammer, K.P. (Eds.), Shock-Wave and High Strain Rate Phenomena in Materials. Marcel Dekker, New York, p. 1075i.

Kim, B.-N., Wakayama, S., Kawahara, M., 1996. Characterization of 2-dimensional crack propagation behavior by simulation and analysis. Int. J. Fract. 75, 247–259.

Kohlhoff, S., Gumbsch, P., Fischmeister, H., 1991. Crack-propagation in bcc crystals studied with a combined finite-element and atomistic model. Philos. Mag. A—Phys. Condens. Matter Struct. Defect Mech. Propert. 64 (4), 851–878.

Lee, Y., Prakash, V., 1999. Dynamic brittle fracture of high strength structural steels under conditions of plane strain. Int. J. Solid Struct. 36, 3293–3337.

Liu, Y., Kageyama, Y., Murakami, S., 1998. Creep fracture modeling by use of continuum damage variable based on voronoi simulation of grain boundary cavity. Int. J. Mech. Sci. 40 (2–3), 147–158.

Luo, J., Stevens, R., 1997. The role of residual stress on the mechanical properties of Al_2O_3—5 vol.% SiC nanocomposites. J. Euro. Ceramic Soc. 17, 1565–1572.

Miller, O., Freund, L., Needleman, A., 1999. Modeling and simulation of dynamic fragmentation in brittle materials. Int. J. Fract. 96 (2), 101–125.

Miller, R., Tadmor, E., Philips, R., Ortiz, M., 1998. Quasicontinuum simulation of fracture at the atomic scale. Model. Simulat. Mater. Sci. Eng. 6, 607–638.

Mullen, R., Ballarini, R., Yin, Y., Heuer, A., 1997. Monte Carlo simulation of effective elastic constants of polycrystalline thin films. Acta Mater. 45 (6), 2247–2255.

Needleman, A., 1988. Material rate dependence and mesh sensitivity in localization problems. Comput. Meth. App. Mech. Eng. 67, 69–85.

Onck, P., Van der Giessen, E., 1999. Growth of an initially sharp crack by grain boundary cavitation. Mech. Phys. Solid 47, 99–139.

Ortiz, M., Pandolfi, A., 1999. Finite-deformation irreversible cohesive elements for three-dimensional crack-propagation analysis. Int. J. Numer. Meth. Eng. 44 (9), 1267–1282.

Ostoja-Starzewki, M., 1998. Random field models of heterogeneous materials. Int. J. Solid Struct. 35 (19), 2429–2455.

Ostoja-Starzewki, M., Wang, X., 1999. Stochastic finite elements as a bridge between random material microstructure and global response. Comput. Methods Appl. Mech. Eng. 168, 35–49.

Sternitzke, M., 1997. Review: structural ceramic nanocomposites. J. Euro. Ceram. Soc. 17, 1061–1082.

Tasker, P., Duffy, D., 1983. Computer simulation of $\langle 0\,0\,1\rangle$ tilt grain boundaries in nickel oxide. Philos. Mag. A 47 (L45).

Tvergaard, V., Hutchinson, J., 1988. Microcracking in ceramics induced by thermal expansion or elastic anisotropy. J. Am. Ceram. Soc. 71 (3), 157–166.

Tvergaard, V., 1990. Effect of fibre debonding in a whisker-reinforced material. Mater. Sci. Eng. A 125, 203.

Underwood, E., 1970. Quantitative Stereology. Addison-Wesley, Reading, MA.

Weibull, W., Sweden, S., 1951. A statistical distribution function of wide applicability. J. App. Mech. 18, 197–293.

Wolf, D., 1984. On the relationship between symmetrical tilt, special, and favored, grain boundaries. J. Phys., Colloque C4, Supplement au 4 (46), C4–197.

Wu, M., Niu, J., 1995a. Micromechanical prediction of the compressive failure of ice: model development. Mech. Mater. 20, 9–32.

Wu, M., Niu, J., 1995b. Micromechanical prediction of the compressive failure of ice: numerical simulations. Mech. Mater. 20, 33–58.

Xu, X.-P., Needleman, A., 1994. Numerical simulations of fast crack growth in brittle solids. J. Mech. Phys. Solid 42 (9), 1397–1434.

Xu, X.-P., Needleman, A., 1995. Numerical simulation of dynamic interfacial crack growth allowing for crack growth away from the bond line. Int. J. Fract. 74, 253–275.

Zavattieri, P., 2000. Computational modeling for bridging size scales in the failure of solids. Ph.D. Thesis, Purdue University, West Lafayette, IN.

Zavattieri, P., Espinosa, H., 2001. Grain level analysis of crack initiation and propagation in brittle materials. Acta Mater. 49 (20), 4291–4311.

Zavattieri, P., Espinosa, H., 2002. An examination of the competition between bulk behavior and interfacial behavior of ceramics subjected to dynamic pressure-shear loading. J. Mech. Phys. Solids, in press.

Zhai, J., Zhou, M., 2000. Finite element analysis of micromechanical failure modes in a heterogeneous ceramic material system. Int. J. Fract. 101 (1/2).

Zhou, M., Zhai, J., 1999. Modelling of micromechanical fracture using a cohesive finite element method. In: F. M.D., C. L.C., and H. R.S. (Eds.), Shock Compression of Condensed Matter, pp. 623–628. APS.

Zikry, M., Kao, M., 1996. Inelastic microstructural failure mechanisms in crystalline materials with high angle grain boundaries. J. Mech. Phys. Solid 44 (11), 1765–1798.